Lab on a Chip

CRITICAL REVIEW

View Article Online
View Journal | View Issue

Cite this: *Lab Chip*, 2023, **23**, 1034

Fluidics for energy harvesting: from nano to milli scales

Nan Wu, Youcef Brahmi and Annie Colin *

A large amount of untapped energy sources surrounds us. In this review, we summarize recent works of water-based energy harvesting systems with operation scales ranging from miniature systems to large scale attempts. We focus particularly on the triboelectric energy, which is produced when a liquid and a solid come into contact, and on the osmotic energy, which is released when salt water and fresh water are mixed. For both techniques we display the state of the art understanding (including electrical charge separation, electro-osmotic currents and induced currents) and the developed devices. A critical discussion of present works confirms the significant progress of these water-based energy harvesting systems in all scales. However, further efforts in efficiency and performance amelioration are expected for these technologies to accelerate the industrialization and commercialization procedure.

Received 8th October 2022,
Accepted 16th December 2022

DOI: 10.1039/d2lc00946c

rsc.li/loc

1 Introduction

A large amount of untapped energy sources surrounds us. They derive from human activities or come from ambient energies such as chemical, thermal, radiant and mechanical energies. Energy harvesting from environment is not recent: people have been harvesting energy for centuries at large scale with windmills and nowadays with wind turbines or photovoltaic batteries. After the radiant sources (sun, RF, *etc.*), mechanical energy (vibrations, wind, rain, *etc.*) and salted gradient are the second main environmental source of energy[1–4] The mixing of 1 cm^3 of sea water with 1 cm^3 of river water produces an energy of 1.4 J.[5] The energy of a rainwater drop falling on a surface is of the order of magnitude of 10 μJ (speed of the drops estimated to 1 m s^{-1}). These energies are not negligible and are comparable to the energy demand for powering current electronic devices. It takes 1 mJ to send a text message and 1 μJ to measure a temperature.[6,7] It seems therefore interesting to develop new techniques to recover energy from water by focusing on the mechanical energy contained in the drops of rain, in waves and in a more original way, in the osmotic energy contained in salt solutions. In such an approach, the first goal will be to be

ESPCI Paris, PSL Research University, MIE-CBI, CNRS UMR 8231, 10, Rue Vauquelin, F-75231 Paris Cedex 05, France. E-mail: annie.colin@espci.psl.eu

Nan Wu

Nan Wu received her bachelor's degree and master's degree from Beihang University. She received her general engineering degree from Ecole Centrale de Lyon. She currently holds a position as a Ph. D candidate at the laboratory of Matériaux Innovants pour l'Energie (MIE) in ESPCI-Paris at Paris Sciences & Lettres University (PSL). Her research focuses on developing innovative and efficient blue energy harvesting systems, especially enhancing energy harvesting efficiency of capacitive reverse electrodialysis systems. Her research interests include energy harvesting systems, capacitive reverse electrodialysis and capacitive electrodes.

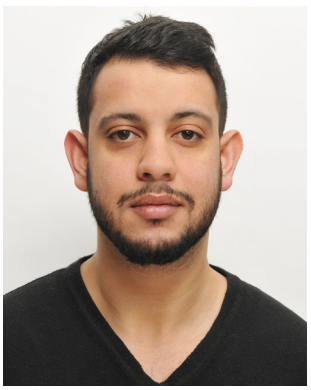

Youcef Brahmi

Youcef Brahmi received his Master degree in Chemical engineering from Ecole Nationale Polytechnique of Algiers and his PhD in physics and chemistry of material from PSL University in 2021. He is currently a post-doc researcher at ESPCI Paris PSL. His research work deals with electrochemistry, materials characterization, chemical engineering and device development.

able to power sensors and embedded electronic devices, which is part of the energy harvesting field. The second goal in the longer term, if the results are there, will be to extend these devices to large scales in order to generate new renewable energy sources to fight against climate change and replace fossil fuels. Researchers estimate that the worldwide salinity gradient energy could reach 2.4–2.6 Terawatts considering all the rivers and effluents running to the sea, among which 1 Terawatt is extractable.[8,9]

In this context, nanofluidics, microfluidics and millifluidics can have an impact in the field of research and development of new strategies to recover blue energy or energy from rain water. Nanofluidics, microfluidics and millifluidics encompasse all techniques for manipulating fluids at nanometer scale (between 1 and 1000 nanometers), micron scale (between 1 and 1000 micrometers) and millimeter scale (between 1 and 1000 millimeters), respectively.

In this review, we focus on emerging techniques for energy harvesting from fluids. In all cases, these techniques involve charge separation mechanisms and the creation of an ionic flow which is then converted into electronic flows either through a capacitive system or a faradic system. The charge separation mechanism is a basic key point in this framework. It remains to this day an open question although much progress has been made recently.[10] It involves the interactions between liquids and solids and the electrification of the contact. In this context it finds its explanations in the mechanics that govern triboelectric phenomena.[11,12]

The remaining part of this review proceeds as follows. In the second part, we will mainly focus on triboelectric energy harvesting systems. We will start with the state of art charge separation mechanisms taking place in liquids, or at the contact between a liquid and a solid surface due to the supply of mechanical energy. Based on these principles, innovative devices for the recovery of the mechanical energy of raindrops or waves are presented. A brief discussion on economic viability is provided at the end of this part. The third part will deal with the recovery of osmotic energy from salted gradient. Here we will present the main techniques including pressure retarded osmosis, reverse electrodialysis, capacitive mixing and capacitive reverse electrolysis. Present technological challenges and economic evaluations of these techniques are discussed in this part. A comprehensive conclusion, which summarizes the present research advancement as well as encouraging perspectives in this field, is provided at the end.

Annie Colin

Annie Colin is a professor at ESPCI Paris PSL and director of the Institut Pierre Gilles de Gennes. She is internationally recognized for her original contributions in the field of soft matter, rheology, materials for energy and microfluidics through her 160 papers and 15 patents.

2 Triboelectric energy harvesting

When two materials or a material and a fluid come into contact by friction, the materials and the fluid become electrically charged. This effect, known since ancient Greece, is called the triboelectric effect. Despite the fact that it is observed on a daily basis, it has only recently been partially explained. In the following section we will clarify this point and in particular illustrate the recent work that explains charge separation. It is possible to take advantage of this phenomenon to create an electric current. The presence of triboelectric charges on the dielectric surfaces can be a force that pushes the electrons in the electrode to flow in order to balance the electric potential drop created. Based on this observation, Wang invented TriboElectric NanoGenerators (TENGs).[13,14] In the second subsection of this part we will see how these devices work by focusing on devices that consist of a liquid and a material. The last subsections are devoted to economic analysis and perspectives of TENGs.

2.1 Contact electrification and charge electrification

2.1.1 Charge separation in liquid due to the amplification of an instability: Lord Kelvin's experiments. The pioneering work of charge separation process in liquids is the well-known Lord Kelvin's experiment. A Kelvin dropper[15] is a device that converts the gravitational potential energy of the drops into a high electrostatic voltage. Two positive feedback loops are constructed in the system to enable continuous ion separation. It consists of a tank equipped with two metallic tubes, two metal rings and two metallic canisters. The canisters are connected to the rings (see Fig. 1) in a well defined way: each canister is connected to the ring that does not feed it. The water drops fall from the two outlets above the conductive rings. When a drop is emitted from the outlet of the capillary nozzles, it has a small charge. The value and the sign of this charge depend on the material of the tube and on the value of the local electric field at the level of the nozzle. Suppose a drop is of positive charge. The metal reservoir will become positively charged as well as the ring facing the second capillary. Drops emitted from the second capillary will be negatively charged and be accumulated in the reservoir connected to the first ring. The phenomenon will be amplified. In a few seconds a voltage difference of several kiloVolts appears between the two tanks. This voltage difference can be so large that it can reach the field breakdown threshold of the air between two plates of a capacitor connected to the two reservoirs. Sparks may appear.

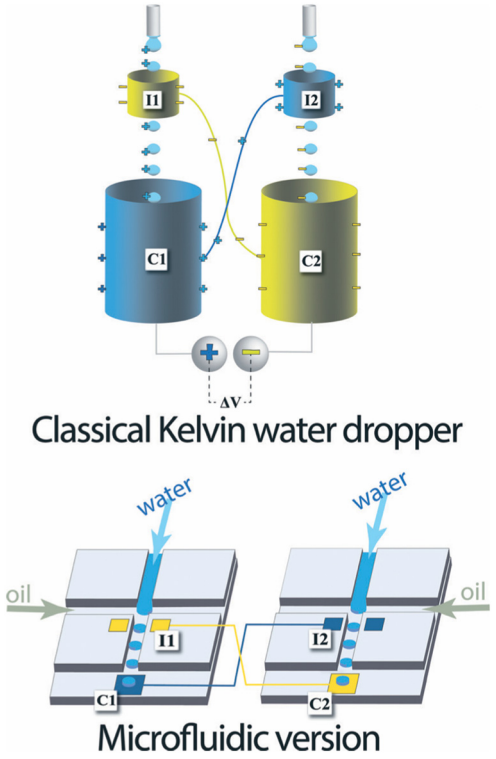

Fig. 1 Top, classical Kelvin water dropper, bottom, representation of the microfluidic version (figures and captions reproduced from ref. 16 with permission from Royal Society of Chemistry, copyright 2013).

This experiment was designed by Lord Kelvin to reproduce the appearance of electrostatic phenomena during thunderstorms. It is to mention that there is no electrical power generated in this system. No electrical currents are involved in the whole procedure, neither of capacitive nature, nor of faradic nature.

At the end of the 20th century, this experience was redesigned to increase the recoverable energy density. Marin *et al.*[16] proposed a microfluidic version of the device in 2013. The device consists of two microfluidic drop generators on different chips. Each chip comprises two types of electrodes: an electrode analogous to the ring of the Kelvin system close to the emission zone of the drops and an electrode further on the channel which recovers the charges. They demonstrated a successful formation of charged liquid drops by this microfluidic system.

2.1.2 Charge separation on graphene. Charge separation phenomena have also been demonstrated by studies on moving drops on graphene.[17,18] The physical mechanism in charge of the production of this electric current has been discussed in many works. It seems to date that a clear picture appears[19] thanks to Density Functional Theory simulations (see Fig. 2). While an ionic liquid drop is deposited onto a graphene surface, cations including H_3O^+ and hydrated Na^+ are preferentially adsorbed on the graphene surface, attracting electrons to accumulate on the upper side of the graphene. This excess of charge under the drop creates a positive charge (an electron deficiency) in the graphene

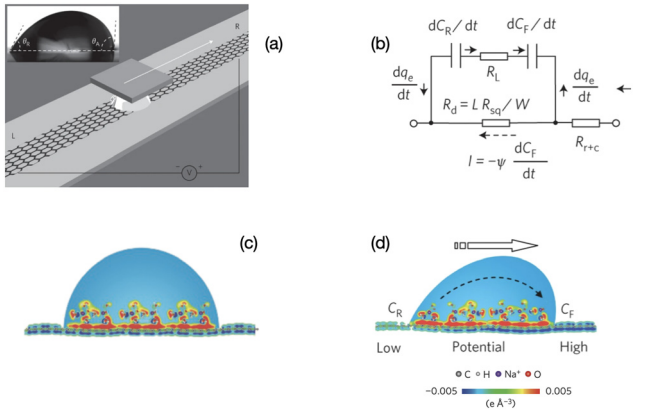

Fig. 2 Mechanism of charge separation on graphene. (a) Illustration of the experimental set-up. A liquid droplet is sandwiched between graphene and a SiO_2/Si wafer, and drawn by the wafer at specific velocities. Inset: A droplet of 0.6 M NaCl solution on a graphene surface with advancing and receding contact angles of 91.98° and 60.28°, respectively. (b) Equivalent circuit for (d). (c) Schematic illustration of the pseudo-capacitance formed by a static droplet on graphene. (d) Schematic illustration of the potential difference induced by a moving droplet (figures and captions reproduced from ref. 19 with permission from Springer Nature, copyright 2014).

which is distributed on the edges of the drop. When the drop does not advance, there is no potential difference created.

When the drop moves, there is a constant supply of positive charge towards the front of the drop. Thus there is a constant supply of electrons at the front interface. Similarly, there is a constant departure of electrons from the back of the drop. These two phenomena induce an electric current in the graphene and a potential difference between the front and the back, with the electric potential at the front being higher than the electric potential at the back. The density power[19] is 19.2 nW cm^{-2} which corresponds to an efficiency of 1%.

Charge separations have also been demonstrated when a graphene-covered surface is dipped in an electrolyte[20] (see

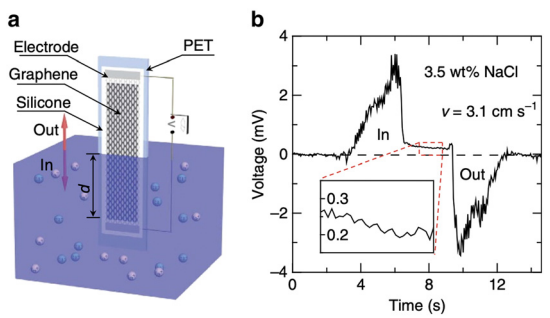

Fig. 3 a, Schematic illustration of the experimental set-up: moving the graphene sample on a polyester terephthalate substrate vertically across the water surface within a container. All the edges of the graphene sheet and silver emulsion electrodes are protected with silicone. b, Typical voltage signals produced as a sample is inserted and pulled out of 0.6 M NaCl solution (3.5 wt%) at a velocity v = 3.1 cm s^{-1} (figures and captions reproduced from ref. 20, with permission from Springer Nature copyright 2014).

Fig. 3). The sodium ions in the electrolyte adsorb rapidly on the surface. Chlorine ions move less rapidly towards the surface from which they are repelled. It therefore takes time to cancel this charge separation. During this time, the electrons in the graphene move closer to the sodium ions, creating holes in the graphene. A difference in the concentration of holes appears along the material and thus leads to the creation of a potential difference and an electric current. When the plate is removed from the liquid, the opposite phenomenon occurs, resulting in an electronic current in the opposite direction. Maximum voltages of 100 mV and maximum currents of 11 μA are measured for surfaces of 20 cm^2. The powers are therefore very low. The authors consider that their work can have an impact in the field of sensors.

At this stage we are not aware of any development of these graphene-liquid systems leading to real efficient devices. However, these new reflections have the merit to improve the understanding of the electrification phenomena. To conclude this section, in the above-mentioned graphene-based charge separation processes, graphene itself presents no permanent static surface charges. The electric current is generated by potential differences and dynamic concentration imbalances. In the following, we will present several charge separation mechanisms involving the creation and use of charged surfaces.

2.1.3 Charge separation and electrification of the liquid/solid contact. The electrification of a contact corresponds to the appearance of charge when two solids or a solid and a liquid are placed in contact. Although known since ancient Greece, the nature of the charge carrier electrons or ions during electrification remains a debate. Using ferrimagnetic solids, Lin *et al.*[21] show that electrification by liquid–solid contact is sensitive to magnetic fields. This result allows to answer the nature of the charge carrier during the contact electrification for ferrimagnetic solids. Indeed, potential charge carriers such as OH^- and H_3O^+ are all in a singlet ground state. They have an extremely weak response to magnetic fields and should not induce a sensitivity of the contact electrification (CE) to magnetic fields. Conversely, the electron spin is sensitive to magnetic field. The transfer of electrons between two species is spin conservative and follows the Pauli exclusion principle. Therefore, the liquid–solid CE should depend on the spin and therefore on the magnetic field if electrons are the charge carriers. These results provide strong evidence that the charge carrier is the electron during electrification of the liquid–solid contact for ferrimagnetic solids. However, these experiments do not allow us to totally reject the participation of ions in the electrification of the contact, especially in the case of other solids such as oxide surfaces or polymers. In recent studies, Lin and his colleagues[10,22] have shown, by performing thermionic emission experiments, that both electrons and ions transfer during the contact electrification between the SiO_2 and deionized water. The electronic transfer corresponds to 75% of the charge transferred in this context. The other 25% corresponds to the reaction between OH^- and SiO_2 which leads to the creation of SiO^-. When the pH is increased to 11 or decreased to 3 the electron transfer remains present but decreases while the ion transfer increases. The electrons transferred to the surface come from the water molecules. This requires during the contact to make appear in a very temporary way ions of type H_2O^+. The existence of the latter is explained by the hybrid layer model of Wang[23] and has been indirectly demonstrated recently by the production of OH radicals and hydrogen peroxide during contact electrification.[24] The surface charges carried by other oxyde[25] or PTFE after contact with water can be explained in the same way. Some of them come from the adsorption of ions during the contact (OH^- adsorption), others from an electron transfer from water to the material.[10]

The electrification of the contact allows to create currents. Let's consider the contact between PDMS (polydimethylsiloxane) and copper lubricated by water. The set-up developed by Lin *et al.*[26] to study this process, encompasses a PDMS layer on which a pyramid-shaped structure has been lithographically etched, a layer of water and a poly(methyl methacrylate) (PMMA) plate covered with a copper film (see Fig. 4). At initial state, a drop of DI water is placed onto the copper thin film, which is noted as electrode 1. For electrode 2, the structured side of the PDMS film is facing the electrode 1, while the other side is covered with a copper thin film. A drop of DI water is deposited onto electrode 1 on the copper surface. When the PDMS comes into contact with the liquid, the ionization of these surface

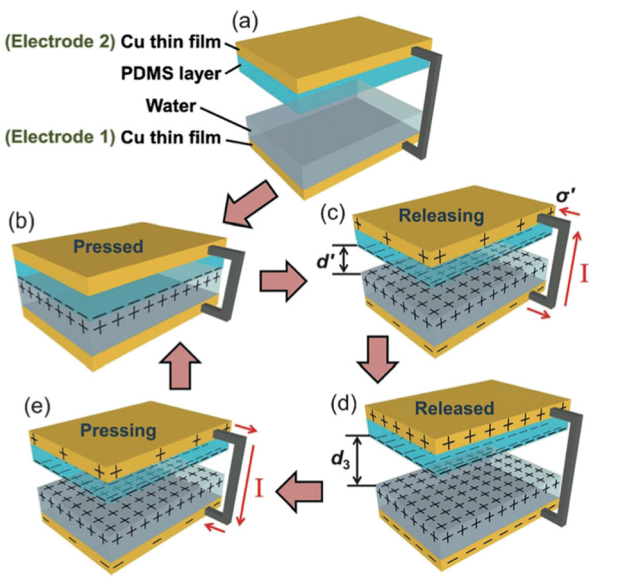

Fig. 4 Working mechanism of the water-TENG. (a) Initial status without any external force applied. (b) External force brings the PDMS layer into contact with water. (c) Removing the PDMS layer from the water surface. (d) PDMS layer returning back to the original position. (e) External force applied makes the PDMS layer contact with water again. For simplification, both PMMA substrates are not shown (figures and captions reproduced from ref. 26) with permission from John Wiley and Sons, copyright 2013.

groups induces the appearance of a positive surface charge in the liquid volume and a negative one on the polymer surface.

When the PDMS is removed from the liquid, its hydrophobic character induces the charge separation. The PDMS carries a net negative surface charge and the liquid a positive charge. This charge is greater the more easily water is drained from the PDMS surface. As said before, the hydrophobic character of PDMS is fundamental to ensure charge separation. A maximum surface charge is generated when the water is completely drained from the PDMS surface in an ideal case. If the two copper films are electrically connected, a flow of electrons occurs between the copper film covered by the PDMS which is negatively charged and the copper film covered by the water drop which is positively charged so as to counterbalance the charges. When the PDMS re-enters the liquid, its charge is locally neutralized by the charge of the liquid. Thus the electrons make the opposite path, results in a capacitive current in the opposite direction. This new prototype of triboelectric contact by charge exchange between a solid surface and a liquid surface produces a current of 2.45 mA m^{-2}, a peak voltage of 52 V and a peak power (not average) of 0.13 W m^{-2} which allows to power 60 LEDs simultaneously. It is worth to be noted that the measured effect strongly decreases when deionized water is replaced by salt water. The power decreases by a factor of 4 when the authors use a 0.6 M NaCl solution instead of deionized water. This explanation is suitable for a surface carrying ionizable groups but is not satisfactory on PTFE surfaces or oxide surface. In this last situation, the interaction of the ions of the solution with the surface is put forward.

Surface charge, wherever it comes from (electrons from water or ions adsorption), seems also to be at the origin of the production of charged drops. We have just seen that the contact of a drop of water on a surface can create surface electrostatic charges and induced currents. A similar mechanism can occur when a liquid flows over a surface. The electrification of the drop after its emission from a nozzle or a capillary has generated a lot of activities over the past 20 years. The surface of the nozzle or capillary[27] has a surface charge.[28] When liquid flows, it will first take away the released counterions which balance the surface charge and reveal a charged surface. Then through the capillary or the nozzle, a layer of counterions will build up at the liquid–wall interface. The whole wall of the tube, electrolyte in the tube is neutral. However, the tube wall and the electrolyte each carry a surface charge which is opposite. The value of the charge depends on the pH, the concentration of electrolytes, the capillary coating and little on the humidity value. This explains why the drops coming out of a capillary are charged. This natural electrification of the droplets does not come from pre-existing free charges on the capillaries but from a charge separation mechanism between a droplet and the surface of the pipette tip which carries a static electric charge. The chemical balance of the surface is not affected by the flow. This causes the upper liquid upstream of the capillary to become inversely charged. The existence of charged drops will be used in the following to generate energy producing devices.

2.2 Applications to energy harvesting devices

2.2.1 Ballistic electrostatic generator. Xie *et al.*[29] developed a device that converts the inertial energy of jet drops into electric current. The device is depicted in Fig. 5. A jet of water is formed at the outlet of a pore of about thirty micrometers in diameter under the action of a strong over-pressure of the order of 100 kPa. Under the effect of Rayleigh Plateau instability, the jet breaks into small drops. These drops possess an electrical charge which is induced by the surface charge of the hole (see above subsection for more details). The charged drops arrive on the target plate which is connected to the ground. In this device, the acceleration of the drops compensates the electric field created between the bottom plate and the electrode. A current of electrons from the ground to the target plate is established. This current is counterbalanced by a current of electrons from the membrane to the ground (see Fig. 5). This device resembles Lord Kelvin's device. However, there are significant differences that make it more efficient. In Kelvin's drop generator, gravity opposes the electric force that slows down the drops, in this device it is the acceleration of the drops. This fundamental difference coupled with the fact that the charges of the drops are 10^4 larger than those of the Kelvin experiment results in higher currents.

The authors claimed that the system displays a conversion efficiency up to 48% and may generate a power density of 160 kW m^{-2} if scale up holds. These figures are excellent. However, although promising, the device is far from being developed as an application. The main disadvantage of this system is that it does not provide for a surface discharge phase. Indeed, in order to produce energy in a system that induces ion flows and then capacitive electron flows, it is necessary either to imagine a process that induces reverse flows, or to set up reactions that consume the charges produced by faradaic reactions. In other words, it is necessary to manage to discharge the surfaces, to depolarize them in order to be able to cycle as in the case of triboelectric systems. Moreover, even if this problem is solved, the system will face the same energy storage problem as triboelectric systems. This system has a very small output impedance and the energy transfer efficiency will be very low. This work has not led to any application developments in the literature but as we said before it is one of the most promising.

2.2.2 Harvesting the rain droplets energy. In this spirit, Xu *et al.*[30] have developed a device that is closer to the application domain. The device consists of several layers of electrodes. An aluminum electrode is placed onto a polytetrafluoroethylene (PTFE) electret, below which an indium tin oxide (ITO) electrode is placed on a glass surface and does not receive liquid drops. It is important to mention the direct connection between aluminum electrode and ITO

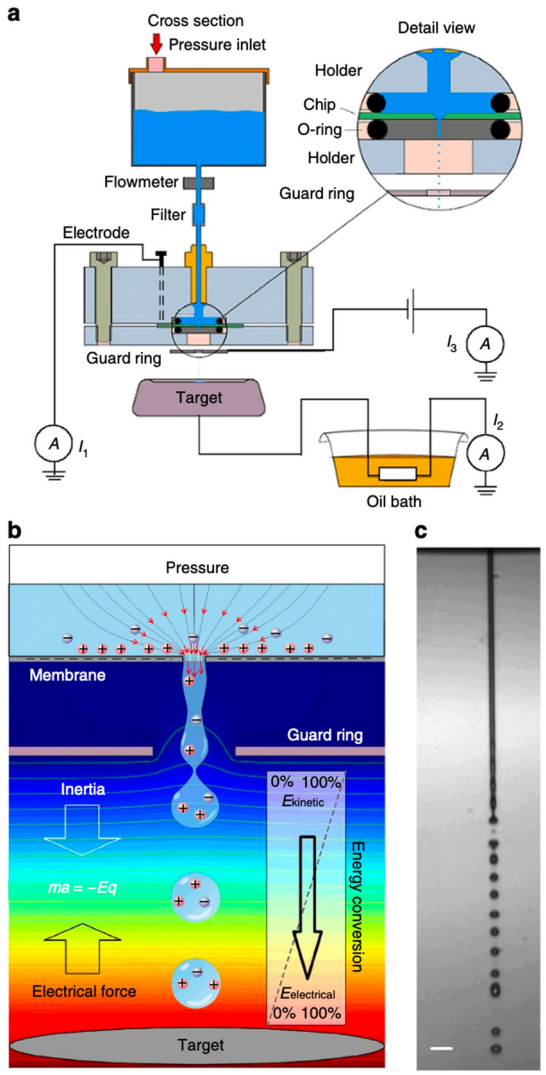

Fig. 5 Concept of energy conversion and set-up. a, Experimental set-up. Aqueous solution is forced by applied air pressure through a 10 or 30 mm diameter circular pore in a 500 nm-thick silicon nitride membrane. A platinum electrode sputtered on the backside of the chip (30 mm pore experiments) or an inserted platinum wire (10 mm pore experiments) was connected to a picoammeter (Keithley 6485). A microjet is formed that breaks up in a droplet stream. The droplets travel through the air and arrive on a metal target placed at 7.5–25 mm distance from the pore opening. The target is connected to electrical ground *via* a high-load resistance. A metal guard ring with an opening of 2 mm diameter is placed at 1.5 mm (10 mm pore) or 5.0 mm (30 mm pore) from the pore exit and maintained at ground potential, or at a negative potential for inductive droplet charging. The current can be measured between ground and the platinum reservoir electrode (denoted I_1), between target and ground (I_2) and between metal guard ring and ground (I_3). b, Conceptual illustration of the conversion principle. Water is accelerated to form a microjet that breaks up into charged droplets. On their air trajectory towards the target, the droplets are decelerated by the electrical force, converting kinetic energy into electrical energy. The background colour from red to blue indicates the voltage distribution from high to low, the lines denote equipotentials. c, Photomicrograph of the microjet from the 10 mm pore taken by double iLIF illumination. Scale bar, 40 mm (figures and captions reproduced from ref. 29 with permission from Springer Nature, copyright 2014).

electrode. This work is directly related to the previous part dealing with electrification by contact between the drops of water and the PTFE. After the impact of $1.6.10^4$ drops (ion concentration 3.1 mM salt), the PTFE reaches a steady charge of 49.8 nC.[31] At steady state, when new drops fall, a resistive water bridge closes an electrical circuit which includes the capacitor created by the electret, the capacitor created by the PTFE/water contact and the capacitor created by the aluminum/water contact (see Fig. 6). These last two being very important compared to the capacity of the electret, the transfer of charge in a closed circuit allows the passage of all the electret charges towards the aluminium water contact. When the drop retracts, the water-aluminium capacity goes to zero and the charges return to the electret. This mechanism includes cyclic procedures where positive and negative capacitive currents are generated. The reversibility is confirmed by the measurement of cyclic charge. An instantaneous peak power density of 50.1 W m^{-2} is reported in this work. The theoretical basis of energy production is presented in detail in ref. 32. The average energy-conversion efficiency of device, defined as the harvested electrical energy relative to the input energy of an impinging droplet, is calculated to be roughly 2.2%. This is several orders of magnitude higher than that of the control device without an aluminium electrode.

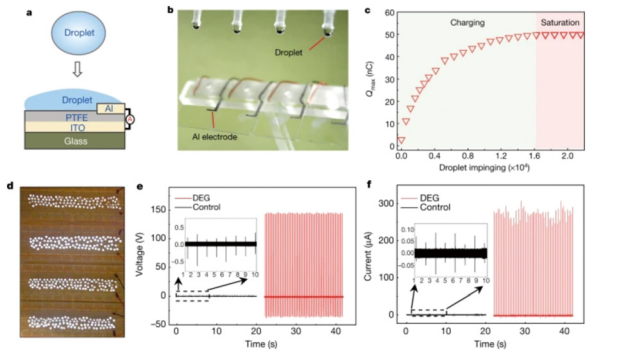

Fig. 6 Schematic illustration of droplet-based electricity generator (DEG). (a) Schematic diagram. (b) Optical image showing four parallel DEG devices fabricated on a glass substrate. The volume of each droplet is 100.0 μl. (c) As individual droplets continue to impinge on the as-fabricated device, the amount of charge on the PTFE surface increases gradually and eventually reaches a stable value. (d) One hundred commercial LEDs can be powered when one droplet, released from a height of 15.0 cm, is in contact with the device. (e) Under the same experimental conditions (for example, the same droplet size and height of release), the output voltage measured from the DEG (in red, with the frequency of impinging droplets being set at 4.2 Hz, and the total number of droplets being about 84) is more than two orders of magnitude higher than that from the control device (in black, with a droplet frequency of 1.0 Hz, and a total of 20 impinging droplets). The negligible electricity generation from the control device is limited by the interfacial effect, although its PTFE surface is loaded with the same amount of charge as the DEG. (f) Comparison of output current from the DEG (in red) and the control device (in black) in response to continuous impinging of individual droplets (figures and captions reproduced from ref. 30 with permission from Springer Nature, copyright 2020).

At this stage we are not aware of the industrial development of this device. The electrification of liquid–solid contacts, that is to say the triboelectric process, is the technique closest to applications and commercialization. We will describe these points in the next subsection.

2.2.3 Harvesting energy of waves. Liquid–solid triboelectric technology is used to collect the energy of waves. A device involving the electrification of a liquid–solid contact was developed by Wang and collaborators[33] to recover wave energy. The material used is a film consisting of PTFE nanoparticles (see Fig. 7). Due to the hydrophobicity of PTFE, the contact angle with water is 110°.

When the water comes into contact with the PTFE, the latter acquires a permanent electrostatic surface charge as explained above in the text.[31,49] During the following phases when the water advances on the surface, the positive ions it contains are adsorbed on the PTFE due to the existence of negative surface charge. As seawater propagates over the surface, this creates a charge gradient on the material, with the emerged part having zero charge and the dry part carrying an unbalanced negative charge. (see Fig. 8). Electrons move away from electrode A whose surface charge is neutralized by the propagating water and head towards electrodes B and C which are both negatively charged (see Fig. 8).

When the water recedes, an electrical reverse current is measured using the same principle. The use of bridge rectifiers makes it possible to recover a current that always flows in the same direction. Thanks to the use of rectifier bridges, it is possible to rectify the current and to sum currents of the same sign, which opens up the possibility of device scaling up. Due to the wetting properties, static charges remain on the PTFE. (We recall that the most probable mechanism responsible for the appearance of this charge is the permanent adsorption of OH^- ions). The authors measure a peak output power of 1.1 mW. This device can power a total number of 10 light emitting diodes.

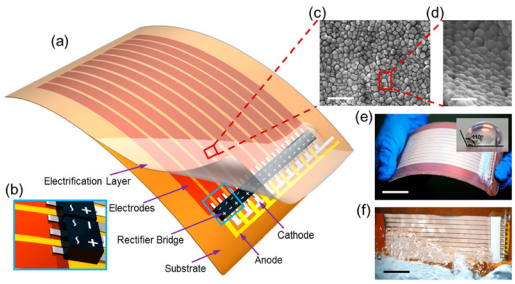

Fig. 7 Structure of a thin-film triboelectric generator (TF-TEG). a, Schematic diagram of an integrated TF-TEG. b, Enlarged sketch of the arrayed bridge rectifiers. c, SEM image of the PTFE nanoparticles on the electrification layer (scale bar = 1 μm). d, Enlarged view of the nanoparticles at a tilted angle of 60° (scale bar = 500 nm). e, Picture of a bendable as-fabricated TF-TEG. Inset: Water contact angle on the nanostructured surface (scale bar = 25 mm). f, Picture of the TF-TEG that is interacting with the water wave (scale bar = 25 mm) (figures and captions reproduced from ref. 33 with permission from American Chemical Society, copyright 2015).

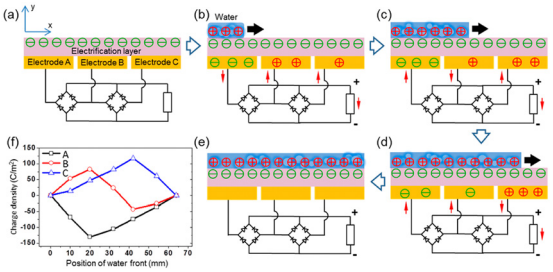

Fig. 8 Electricity-generating process of the TF-TEG. (a) Cross-sectional view of charge distribution when the device is fully exposed from water. Charge distribution when water is propagating across (b) electrode A, (c) electrode B and (d) electrode C. (e) Charge distribution when water fully covers the electrification layer underneath. (f) Charge density on the three electrodes as the water front propagates (figures and captions reproduced from ref. 33 with permission from American Chemical Society, copyright 2015).

In the same spirit, Wang *et al.*[50] have developed a device which recovers the energy dissipated during the navigation on the hull of a boat. The originality of this work, which is complementary to the previous one, consists in the development of a coating that avoids the proliferation of algae and microorganisms on the triboelectric layer. The device has excellent stability and high performance. It allows several LEDs to be illuminated during navigation. Currently, many groups[51,52] are studying PTFE for energy harvesting applications based on liquid–solid contact electrification. This material is one of the most promising. It is possible[38] to recover 3 W m^{-2} in the best conditions.

2.2.4 Harvesting water from unsteady flows. It is possible to generate triboelectric currents in a pipe covered by different materials. Ahn *et al.*[46] inserted a PVDF zone in a silicone tube. They placed a grounded copper electrode on the top of the PVDF zone. A salt water solution circulates in the tube. Silicone and PVDF have different surface charges. Thus the ion concentration in the Stern layer in the vicinity of the Silicone and PVDF is different. During a flow the Stern layers move. The charge in the Stern layer close to the PVDF varies and becomes unbalanced. This causes a current of electrons coming from the ground and trying to cancel the charge separation. When the flow is decreased, the charge concentration in the Stern layer returns to its initial value and a current of electrons in the opposite direction is created. The harvested power reaches 11.5 μW. Using the same approach Cheedarala *et al.*[44] measured a power density of 25 mW m^{-2} with a pulsating flow.

2.2.5 Hybridized triboelectric nanogenerator: coupling charge separation TENG and contact TENG. In the previous examples, the current produced is created by a charge separation mechanism. When a raindrop falls, it brings with it charges but it also brings with it mechanical energy that can produce a current if it causes contact between two solids with different triboelectric properties. A very first approach concerned the coupled recovery of the kinetic energy and the electrostatic energy of water. When a raindrop or water falls, it not only brings charges, but also possesses a large amount

of mechanical energy which can be harvested if a liquid/solid contact with different triboelectric properties is designed. Such idea leads to the creation of hybridized TENGs, where a coupled recovery of kinetic energy and electrostatic energy is realized in a single system. Cheng *et al.*[41] have designed an impeller whose blades are composed of superhydrophobic polytetrafluoroethylene (PTFE) thin films with nanostructures. These PTFE blades are used to harvest the electrostatic energy of the flowing water. The water flowing over the blades turns the wheel and sets in rotation a triboelectric disc that collects the mechanical kinetic energy. At a water flow rate of 54 mL s^{-1}, the device involving electrostatic energy has an open circuit voltage of 72 V, a short circuit current of 12.9 μA, and a maximum power of 0.59 W m^{-2}. To this power must be added the power produced by the conventional disk TENG whose open circuit voltage is 102 V, short circuit current is 3.8 μA and maximum power density is 0.03 W m^{-2}. These results show the potential of liquid–solid contact electrification onshore and offshore and even in rainy areas. Following these considerations, hybrid nanogenerators have been developed[36,48] (see Table 1 for the performances). Recently, a fluorinated ethylene propylene (FEP)-based tribonanogenerator has been coupled to a piezoelectric material (PVDF) mounted on a cantilever. The deflection of the cantilever during the passage of the drop allows to capture the kinetic energy of the drop while the FEP coupled to a metallic electrode allows to recover the electrostatic energy.[45]

2.3 Economic analysis

The levelized cost of electricity LCOE is the cost necessary to produce electricity from a process, taking into account the materials, resources needed for the production, the life time and the maintenance during the process. In 2022, The BloombergNEF report estimates LCOE for onshore wind to be 0.044 $ per kW h and 0.042 $ per kW h for solar PV without storage.[53] The LCOE of storage is estimated in the same report to be 0.146 $ per kW h. The US average LCOE of wind projects built in 2021 was 0.031 $ per kW h.[54] It becomes very complex to give that of gas and fossiles combustible in the context of the war in Ukraine. Before the Ukraine war in 2021, the LCEO of gas was 0.081 $ per kW h.[53] The LCOE of triboelectrical generators has been estimated by Ahmed *et al.*[55] and is comprised between 0.02 and 0.09 $ per kW h. Unsurprisingly, this figure is lower than that for renewable and fossil fuels. The triboelectric devices are made of polymers and conductive layers already very present in the industrial world. The costs of these materials are low. Efficiency and module lifetime are the most sensitive factors for the LCOE of TENG. The lowest value of the LCOE assumes a life time of 15 years. In the same work,[55] the authors evaluated the Energy PayBack Time (EPBT) of a TENG, *i.e.* the time needed to produce the same amount of electricity (converted into equivalent primary energy) with the energy consumed during its life cycle. The two generators used have EPBT comprised between 0.1 and 0.25 year. These

Table 1 A summary of present solid–liquid nanogenerator

Materials	Output current (μA)	Power (μW)	Power density (W m^{-2})	Comments	Ref.
CYTOP	30	10^3	—	Water drops plus electret	34
FEP	2.6	1.2×10^5	—	Water drops, an efficiency of 7.7%	35
FEP-PTFE	5.1 + 4.3	41.2 + 3.03	—	Hybrid TENG (interfacial electrification TENG (IE-TENG) + impact-TENG)	36
HCOENPs-coated fabric-PET	3.2	—	0.14	Wearable all-fabric-based triboelectric generator	37
Graphene	1.7	1.92×10^2	—	Efficiency of 1%	19
PDMS-Cu	2.45×10^3 m^{-2}	—	0.13	Water-TENG	26
PDMS-PTFE	5.5	1.2×10^3	3	Water-TENG	38
PTFE	0.553	1.2	—	Water drops	39
PTFE	17	145	—	Superhydrophobic micro–nanostructured polytetrafluoroethylene (PTFE), water drop contact electrification	40
PTFE	12.9 + 3.8	—	0.59 + 0.03	Hybrid TENG (water-TENG + disk-TENG), water flow rate 54 mL s^{-1}	41
PTFE	13	1.1×10^3	—	Thin-film TENG	33
PTFE-FTO	1.8	—	0.01266	Multi-unit transparent TENG, flow rate 45 mL s^{-1}	42
PTFE-ITO	270	—	50.1	Water drop contact electrification	30
PTFE-nylon	0.54	—	1.838	Bi-electrode freestanding mode TENG (BF-TENG)	43
PVDF-Al	1.67	—	0.02653	Unsteady peristaltic flow induced pulsatile flow-TENG (PF-TENG)	44
PVDF-Al-FEP	6.2	1.34×10^4	—	Coupled TENG and piezo ENG	45
PVDF-BOPP	2.4	11.5	—	Fluid-based TENG	46
PVP	5.3	—	0.5	Power peak to peak, water drops	47
Superhydrophobic TiO_2 + SiO_2	43 + 18	—	1.31 + 0.18	Hybrid TENG (water-TENG + contact TENG), flow rate 40 mL s^{-1}	48

values are lower than those of the solar devices which are included between 0.3 and 2.5 years depending upon the different technologies. TENGs are more efficient and have a smaller energy footprint than photovoltaic cells. Indeed their manufacture does not require to purify and to treat silicon or rare elements necessary to the constructions of photovoltaic cells. These processes consume a lot of energy. A comprehensive analysis points out, that to improve these performances, more efforts should be made to increase the lifetime and the efficiency of TENGs rather than to identify cheaper materials and fabrication processes.

2.4 Perspective dealing with TENG

The results presented in this section are very encouraging and show the potential for commercial applications. The performances of some of these devices are reported in Table 1. The power densities that can be obtained are variable and range according to the experimental conditions from mW m^2 to 50 W m^2. Couplings between different devices (*e.g.* PiezoENG coupling with a Water TENG[45] or a Water TENG coupling with a Solid Contact TENG[36,48]) seem very promising. However, there is still a lot of work to be done to bring these techniques to the commercial level. There is a need to increase the energy conversion at the triboelectric layer level. This requires a better understanding of the physical mechanisms related to triboelectricity. Although triboelectric series have been established for a long time, the study of liquid–solid contacts calls for their modification. This requires research into new materials, new composites involving carbon nanotubes,[56] graphene[57] and systematic studies. These materials must be mechanically resistant, hydrophobic and possess a high surface charge. The energy storage at the device output has to be improved. Indeed, most of these devices have very low output impedances which strongly limit their use in the context of charging a battery or a super capacitor. The capacity of a TENG is very small of the order of 100 pF. These characteristics result in a low energy transfer efficiency, whether for charging a battery or powering electronic devices. These later generally have a much higher impedance (100 of μF). In order to transfer a maximum amount of energy, it is important to insert an electronic stage between the battery or the super capacitor that allows to adapt the impedances. This can be achieved by using N capacitors in series on charge and in parallel on discharge (basic switched capacitor convertor) or a fractal design based switched-capacitor-convertor (FSCC).[58] In the last situation, a energy transfer of 94% with an impedance reduction of 750 has been demonstrated. Last but not the least, the durability of the materials has to be improved. Moreover, it should be noted, that polymer devices are easily corroded by seawater.[59] Thus, some of the wave energy harvesting devices involve fully enclosed TENG devices whose review is beyond the scope of this work.[60–64] The power density of some of these devices[64] may reach 10.6 W m^{-3}.

In the following part, we will focus on osmotic energy harvesting. The technologies for saline gradients recovering emerged earlier and thus are more mature than the above-mentioned ones. There were already several pilot-scale attempts in industrial field, as well as other novel trials planned in the future. Considering the present energy crisis, these osmotic based energy harvesting systems might reach the threshold of economical viability soon.

3 Osmotic energy harvesting

The osmotic energy released during the process of mixing solutions of different salinity is clean and renewable energy. It is nicknamed blue energy.[65,66] Naturally, a spontaneous and irreversible mixing of river water and sea water happens at the estuary, resulting in an entropy increase of the system.[67] A precise and engineering control of this entropy change procedure enables the blue energy harvesting. The potential of blue energy can be estimated by thermodynamics studies. The non-expansion work released from the mixing of seawater and freshwater can be described by the Gibbs free energy of mixing ΔG_{mix} at a constant pressure P and at absolute temperature T.

$$\Delta G_{mix} = G_{mix} - (G_H + G_L) \quad (1)$$

Here, G_{mix}, G_H and G_L represents the Gibbs free energy of brackish water after mixing, seawater of high salinity and freshwater of low salinity, respectively.

As the Gibbs free energy is defined as $G = \sum_{i=1}^{N} \mu_i n_i$, where μ_i and n_i represent the chemical potential and the mole number of species i for a system consists of a number of N species. The chemical potential μ_i is defined as $\mu_i = \mu_i^* + RT \ln(\gamma_i x_i)$ where μ_i^* is the standard chemical potential, R perfect gas constant. γ_i and x_i represent the coefficient of activity and the mole fraction of species i, respectively. For a system of volume V, the molar concentration is defined as $n_i = c_i V$, where c_i is the molar concentration of species i. Thus the Gibbs free energy of mixing can be calculated as:[68]

$$\Delta G_{mix} = \sum_{i=1}^{N} \left[c_{i,mix} V_{i,mix} RT \ln(\gamma_{i,mix} x_{i,mix}) - c_{i,H} V_{i,H} RT \ln(\gamma_{i,H} x_{i,H}) - c_{i,L} V_{i,L} RT \ln(\gamma_{i,L} x_{i,L}) \right] \quad (2)$$

A maximum power of 0.8 W for fresh water of 1 cm^3 is predicted by theoretical calculations,[69] which is equivalent to the hydraulic energy generated by water dams with water falling from 250 m high.[70] Development of efficient and robust energy harvesting technologies is of great importance for the exploitation of this untapped renewable energy. In the following of this section, a review of blue energy harvesting technologies and their applications is explained in details. We first describe pressure retarded osmosis and then move to reverse electrodialysis and to Capmixing and CRED.

3.1 Pressure retarded osmosis

As an emerging energy harvesting system, the technology of pressure retarded osmosis (PRO) is attracting much attention.[71,72] Semipermeable membranes, which allow the passage of water molecules and block the passage of ions, are used in the configuration of PRO systems.[73] To better illustrate the power generation principle of PRO, an introductory explanation of the osmotic process across the semipermeable membrane is given in the following paragraph.

The observation of osmotic phenomenon was firstly documented by Jean-Antoine Nollet. It describes the spontaneous movement of a solvent flux moving across the semipermeable membrane towards a solute of higher concentration, in the way of balancing solute concentrations on both sides of the membrane.[75] The concentration difference across the membrane results in an osmosis pressure difference $\Delta\pi$. Additional hydraulic pressure ΔP could be applied on the system to influence the solvent flux. Description of the water (solvent) flux J_w is an essential parameter in the description of osmotic phenomenon. It can be theoretically described as a function of the applied hydraulic pressure difference ΔP and the effective osmosis pressure difference $\Delta\pi$ for an ideal membrane as $J_w = A_x(\Delta\pi - \Delta P)$. Here A_x refers to the permeability of the membrane.[76]

Based on the comparison between ΔP and $\Delta\pi$, osmotic process can be briefly classified into four categories as illustrated in Fig. 9(a).[74] The Forward osmosis (FO) corresponds to a trivial case where ΔP is zero, indicating no mechanical work in this process. In this case, water flux is driven by the osmotic driving force, penetrating the semipermeable membrane and proceeding to the draw solution side. While applying a hydraulic pressure difference on the feed solution compartment ($\Delta P < 0$), the above-mentioned process is further assisted and accelerated in the so-called procedure of pressure assisted osmosis (PAO). In the case where $\Delta P > \Delta\pi$, the direction of the water flux is reversed (from draw solution to feed solution) due to the external hydraulic pressure. This procedure is named as reverse osmosis (RO) and has intriguing applications in water desalination. It is to mention that both PAO and RO are energy consuming processes. On the contrary, PRO is the only power generating process where the water molecules move from feed solution towards the pressurized draw solution under osmotic effect ($0 < \Delta P < \Delta\pi$). The pressurized solution is then utilized to drive turbine systems for electricity power generation. A complete description of the water flux (J_w) and the power density (W) of each osmotic process is illustrated in Fig. 9(b and c).[74]

Fig. 10 presents a typical configuration of the PRO plant. Feed solution and draw solution are both filtered and pumped into the PRO module. Under the osmotic effect, a water exchange flow rate (ΔQ) is created near the semipermeable membrane moving from feed water side towards draw water side. The brackish water received in the feed water chamber presents a higher flow rate of ($\Delta Q + Q_H$) and a higher hydrostatic pression P_H. The brackish water is then divided into two streams, where one stream is depressurized to drive turbine systems and produce electricity and the other one is delivered into a pressure exchanger to maintain the incoming pressure of draw solution.[77] Here the gross power density of a PRO system can be experimentally calculated as[78]

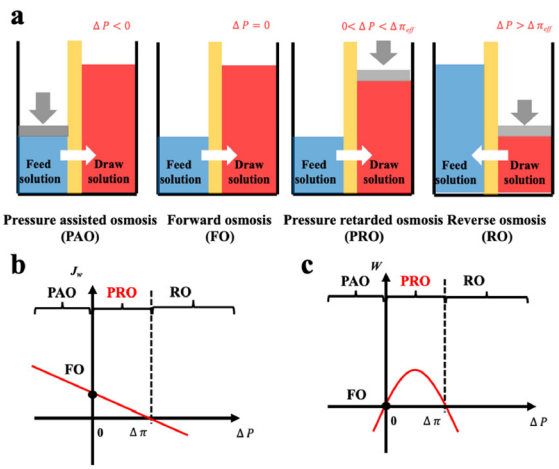

Fig. 9 Schematic illustration a, and analysis b and c, of four classic membrane-based osmotic processes of pressure assisted osmosis (PAO), forward osmosis (FO), pressure retarded osmosis (PRO) and reverse osmosis (RO) (figures and captions reproduced from ref. 74 with permission from Elsevier, copyright 2021).

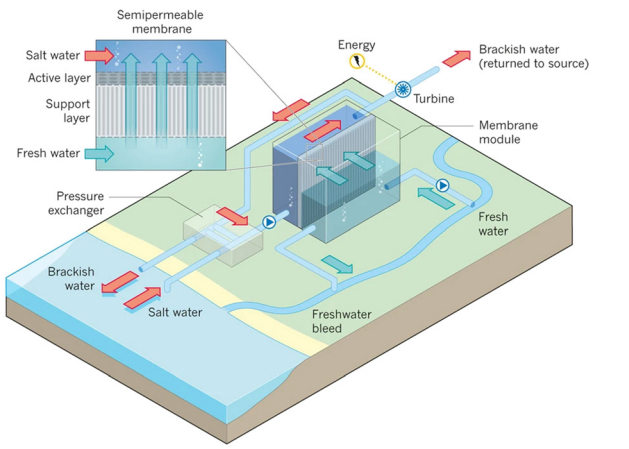

Fig. 10 Schematic illustration of the working principle of PRO systems. Feed solution and draw solution are injected continuously into water compartments which are separated by semipermeable membranes. Driven by effective osmotic force, water flux flows across the membrane from freshwater compartment towards saltwater compartment, resulting in a concentration decrease and a flow rate increase in draw solution compartment. The pressurized water flux is then split into two fluid streams: one fluid stream is used for electricity generation by driving an installed turbine, while the other stream returns to a pressure exchanger to maintain the pressure of draw solution (figures and captions reproduced from ref. 80 with permission from Springer Nature, copyright 2012).

$$P_{\text{gross}} = \frac{\Delta Q \Delta P}{A_{\text{m}}} = \Delta P J_{\text{w}} \quad (3)$$

where A_{m} refers to the effective surface area of the membrane, ΔP refers to the transmembrane hydraulic pressure and J_{w} refers to the water flux across the membrane.[79]

3.1.1 Major challenges in PRO. Although PRO is a promising technology for energy harvesting, PRO modules still suffer from limiting factors in practical use. As illustrated in Fig. 11, a semipermeable membrane is composed of an active layer and a support layer.[74] An ideal membrane is expected to have high water permeability while maintaining a high salt selectivity. However, it was demonstrated in the work of Straub *et al.* the existence of tradeoff between these two factors (Fig. 12(A)).[78]

One of the major obstacles of membrane applications is the polarization effect, which refers to the ion accumulation phenomenon near the semipermeable membrane. The internal concentration polarization (ICP) corresponds to an immobile area clogged with ions in the dense support layer.[81] External concentration polarization (ECP) occurs at the interface between active layer and the draw solution (dilutive ECP) or feed solution (concentrative ECP). Concentration polarization effect deteriorates the osmotic driving force across the membrane, thus leads to lower effective membrane performances and power density output.[82] In addition, the imperfection of membranes could lead to ion leakage from draw solution to feed solution, which is named as reverse salt flux (RSF).[83] The trace leakage might cause more severe ICP effect in the system, lower the power density output, and could possibly promote membrane fouling problems,[84] which is also one of the major limitations on PRO power density output. A theoretical analysis of the impact of ICP and RSF was conducted by Straub *et al.*, as illustrated in Fig. 12(B). An apparent drop in power density is observed under the synergistic effect of ICP and RSF.[78]

Biofouling is a common problem for the industrial application of membranes. It influences severely the membrane performances in practical use, hinders the lifespan of membranes and raises additional fees for water pre-treatment.[85] The mechanical strength of membranes is also the key point for the development of PRO performances and its commercialization.[74]

In general, ideal PRO membranes should reach the following criteria: large water permeability, high salt rejection (high membrane selectivity), low reverse flux, limited biofouling problems and reinforced mechanical strength.[86] Precise engineering of the membrane's properties, including layer thickness, geometry configuration, porosity, selectivity and *etc.*, is summarized in the following paragraph.

3.1.2 PRO membrane development. At the early stage of PRO technology development, commercial membranes developed for RO and FO applications were used. In the pioneer work of PRO, Loeb *et al.*[87] used 'Minipermeators' with asymmetric hollow fibers of Du Pont Permasep B-10 initially developed for RO applications on sea water desalination. Later, Mehta *et al.*[88] realized a series of tests of the commercial membranes for RO and FO applications. Investigations on spiral-wound minimodules of cellulose acetate brackish water membrane and hollow fiber minipermeators were realized. Then the initial cellulose-based membranes designed for PRO applications with superior hydrophobicity and mechanical strength was used in studies.[89] These flat-sheet cellulose acetate membranes, including cellulose acetate (CA) and cellulose triacetate (CTA), were developed by HIT (Hydration Innovation Technology).[90] The early studies indicate a low energy harvesting performance of PRO mainly due to the use of unsuitable and bulky membrane structures, which causes severe ICP effect and reverse water flux problems.[91] In recent years, development in membrane design and surface modification promotes a vast progress for PRO membranes. The present membranes for PRO applications could be classified into two categories: the thin film composite (TFC) flat sheet membranes and thin film composite hollow fiber.[92]

Flat-sheet PRO TFC membranes consist of a highly-porous support layer and an active layer to reinforce its selectivity.[93] Polyamide (PA) is commonly chosen as the active layer, which is polymerized over the interface of the support layer through the phase inversion polymerization.[86] Various works were realized to optimize the permeability and structure integrity, aiming to ameliorate the power density output of PRO systems.

Table 2 lists the present work of flat-sheet PRO TFC membranes in literature.

It was demonstrated that membrane post-treatment of PA active layer could significantly increase the power density of PRO systems. Yip *et al.*[94] compared the performance of membranes with and without NaOCl and $NaHSO_3$ solution immersion and heat treatment. The highest power density output is predicted to be 10 W m^{-2} with proper post-treatment. A detailed study on membrane post-treatment was conducted by Han *et al.*[95] An optimal post-treatment condition was reported to generate a power density of 12 W m^{-2} under a hydraulic pressure of 15 bar. Integrating

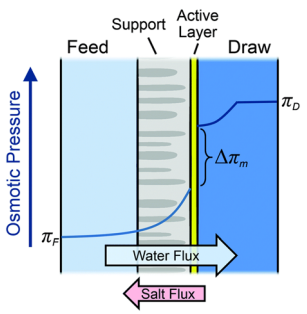

Fig. 11 Illustration of the semipermeable membrane cross section composed of an active layer and a support layer. A qualitative presentation of osmotic pressure profile across the membrane is presented (figures and captions reproduced from with permission ref. 78 with permission from Royal Society of Chemistry, copyright 2016).

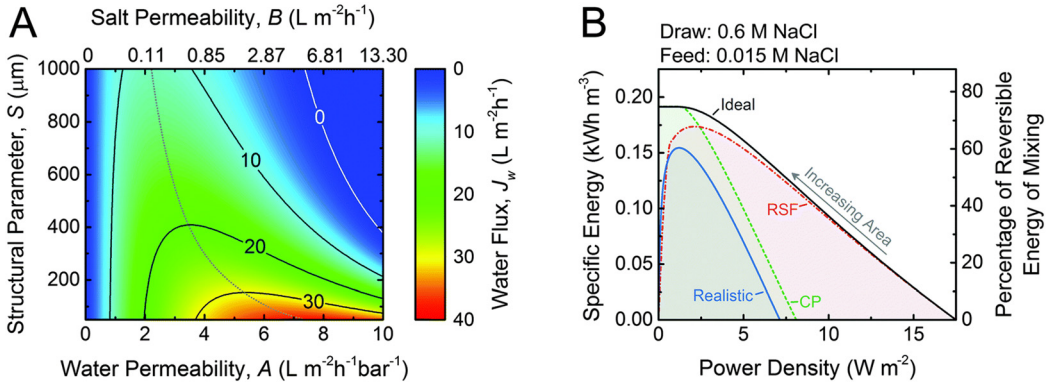

Fig. 12 A. Coupon-scale water flux J_w as a function of the water permeability coefficient, *A*; NaCl permeability coefficient, *B*; and support layer structural parameter, *S*. The water permeability and salt permeability are linked by the permeability-selectivity trade-off. B. Specific energy and power density for counter-current membrane modules with increasing membrane area from right to left. Data for three types of membranes are shown: ideal (solid black line), RSF (dash dotted red line) and CP (dashed green line) and realistic (solid blue line) (figures and captions reproduced with permission from ref. 78 with permission from Royal Society of Chemistry, copyright 2016).

Table 2 A summary of present PRO systems using flat-sheet PRO TFC membranes

Materials	Concentration gradient	Hydraulic pressure (bar)	Power density (W m^{-2})	Comments	Ref.
PA/PSf-PET	DI/0.5 M	12	10	NaOCl, $NaHSO_3$ and heat treatment	94
PA/PI	DI/1.0 M	15	7–12	NaOCl, $NaHSO_3$ and MeOH treatment	123
PA/PAN	DI/3.5% (w/w)	10	2.6	NaOCl and $NaHSO_3$ treatment	124
PA/PAI	DI/3.5% (w/w)	6	2.84	PDA coating and NaOCl, $NaHSO_3$, EtOH treatment	96
PA/PI	DI/1.0 M	9	6.0	PA blended with moderate *p*-xylylenediamine	125
PA/PAN	80 mM/1.06 M	22	15.2	NaClO treatment	126
PA/PI	DI/1.0 M	22	18.1	PA modified with DMF and SDS	127
PA/PAN-PE	DI/0.5 M	11.5	8.0	PA selective layer of mTFC/pTFC	99
CTA membrane	DI/3.0 M	48	60	—	128
PA/PEI	10 mM/1.0 M	17.2	12.8	—	129
PA/PEI	DI/1.0 M	16.9	17.3	Tiered PEI nanofibrous support with multi-walled CNTs	100
PA/PSf-PET	10 mM/1.0 M	18.4	7.1	—	130
PA/PES	DI/0.5 M	6	1.6	CNT-embedded-PES with NaOCl and $NaHSO_3$ treatment	97
PA/PSf	DI/1.0 M	22	12.9	PSf support layer reinforced by PVP	98
PA/PES-PET	DI/1.0 M	25	12.5	—	131
PA/PK	DI/0.6 M	28	6.1	PK reinforced by PED non-woven fabric	132
GO membrane	17 mM/1.0 M	6.9	12.8	—	133
PA/PET	DI/1.0 M	21	12.1	PSf/GO and PSf/HNT (dual layer) nanocomposite on PET	101
PA/TR-PBO	DI/1.0 M	15	17.9	TR-PBO (thermally rearranged polybenzoxazole-co-imide)	104
PA/PAI	DI/1.0 M	21	12.1	PA incorporated with SNW-1 nanocomposite	102
PA/TR-PBO	DI/3.0 M	27	87.2	TR-PBO ESMs exposed to direct fluorination	105
PA/TR-PBO	DI/1.0 M	21	26.6	TR-PBO modified with PVA coating	134
PA/PE	DI/1.0 M	20	35.7	PA formed by toluene-assisted IP	103

additives into support layer is another common strategy applied in membrane research for PRO applications. Li *et al.*[96] realized polydopamine (PDA) modification onto the polyamide-imide (PAI) support layer. Son *et al.*[97] successfully embedded carbon nano tubes (CNTs) into the polyethersulfone (PES) support layer, obtaining a power density output of 1.6 W m^{-2} at a hydraulic pressure of 6 bar, using deionized (DI) water and NaCl solution of 0.5 M. Wei *et al.*[98] realized polysulfone (PSf) support layer reinforced by polyvinylpyrrolidone (PVP), and obtained a maximum power density of 12.9 W m^{-2} at hydraulic pressure of 22 bar.

Flat sheet membranes could also be prepared by electrospun polymeric supports of high porosity and tortuosity. A highly-porous support layer was realized by Bui *et al.*[99] by electrospinning polyacrylonitrile (PAN) nanofibers onto a polyester (PET) fabric substrate. Tian *et al.*[100] prepared tiered polyethylenimine (PEI) nanofibrous support incorporated with multi-walled CNTs. Use of such membrane in PRO system generates a power density of 17.3 W m^{-2}. A dual layer of PSf/GO (graphene oxide) and PSf/HNT (halloysite nanotube) of nanocomposite on PET was prepared by Lim *et al.*[101] to ameliorate water permeability.

The possibility of incorporating nano-sized materials into conventional membranes has been well developed by researchers. Gonzales *et al.*[102] incorporated Schiff base network-1 (SNW-1) nanocomposite into the PA active layer preparation. The PRO system reached its maximum performance of 12.1 W m^{-2} with DI water and brine water of

1M. Kwon *et al.*[103] realized a toluene-assisted interfacial polymerization to fabricate active layer of PA onto a polyvinyl alcohol (PVA)-coated polyethylene (PE) support. An astonishing power density of 35.7 W m^{-2} was reported for a hydraulic pressure of 20 bar. Recently, a Korean research group reported a novel thermally rearranged TFC membrane containing polybenzoxazole-co-imide (TR-PBO) combined with a PA layer.[104] A giant power density increase towards 40 W m^{-2} was reported in its first work. Later, modification with fluorination on TR-PBO membranes ameliorate the output power density towards 87.2 W m^{-2} in PRO applications.[105]

There is no doubt that tremendous advances were achieved in flat-sheet PRO TFC membranes. However, most published works presented here focus on gross power densities, calculated by eqn (3). Actually, the module gross power densities presented here differ from the net power density due to the irrecoverable pumping energy input and the energy losses during electricity generation in turbine systems.[106] Taken into consideration the pumping energy inputs and energy losses, the net power density in published works might be much lower than its gross value. A detailed economic analysis of PRO systems will be given later.

In conventional PRO configuration using flat-sheet membrane, a feed spacer is needed to maintain the feeding channel geometry and reinforce the mass transfer near the membrane.[107] Such configuration decreases the hydraulic pressure and results in an energy loss in the PRO system.[108] In addition, feed spacers might cause membrane deformation at high hydraulic pressure, inducing severe reverse solute diffusion of the membrane and leading to performance loss.[86]

Different from flat-sheet membranes, hollow fiber PRO TFC membranes have a self-supporting tubular shape of higher effective surface area. Such geometry avoids the use of feed spacers, thus limit the deformation failure in flat-sheet based PRO systems. The PRO module using hollow fiber membranes could also achieve a higher pack density, which could efficiently ameliorate output performances.[109] The major preparation method of the hollow fiber membrane is the phase separation spinning, including non-solvent induced phase separation (NIPS) or thermal induced phase separation (TIPS).[77]

The first work dealing with hollow fiber TFC membranes for PRO application was realized by Chou *et al.*[110] They successfully prepared a tubular self-supporting membrane made of PES as the supporting substrate and PA as the selective layer. A maximum power density of 10.6 W m^{-2} could be achieved by using the home-made hollow fiber PRO membrane with a salt concentration of 40 mM and 1 M for fresh and salt water chambers, respectively. The same group prepared a novel hollow fiber TFC membrane using PEI as the supporting substrate.[111] This PEI based hollow fiber membrane presents superior mechanical strength and shows a better power density output of 20.9 W m^{-2} under a hydraulic pressure of 15 bar.

Similar to flat-sheet PRO TFC membranes, chemical modifications on selective layer and the supporting substrate are both widely investigated in the research field. The work of Ingole *et al.*[112,113] proves the effectiveness of PDA coating on PES supporting substrates in PRO applications. A power density increase from 1.62 W m^{-2} to 3 W m^{-2} is realized due to the additional coating. Grafting of chemical groups on supporting substrates were also reported in literature.[114,115]

Ingole *et al.*[116] prepared CA layer treated with tributyl phosphate (TBP) onto the supporting substrate of PES with PDA coating. An improved power density of 3.9 W m^{-2} is achieved with the same brine water and fresh water conditions used in their previous work. Zhang *et al.*[117] reported a novel supporting substrate of PES with PDA coating, grafted with dendritic-architecture sulfonated hyperbranched polyglycerol (SHPG). A superior resistance to protein adhesion and bacterial attachment is achieved due to the high wettability of the polymer brushes. A maximum power density at hydraulic pressure of 15 bar is reported to be 18.8 W m^{-2}.

An emerging trend nowadays is to incorporate nanocomposites into membrane preparation. Zhao *et al.*[118] grafted carbon quantum dots (CDQs) onto the PDA coating of the PES supporting substrate by covalent bonding during the hollow fiber membrane preparation. They obtained a maximum power density of 11 W m^{-2} at a hydraulic pressure of 15 bar. Another work of incorporating CDQs in PA selective layer was realized later by Gai *et al.*[119] They reported a better power density of 34.2 W m^{-2} at hydraulic pressure of 23 bar. Park *et al.*[120] incorporated graphene oxide nanosheets with PES supporting substrate.

In addition, numerous research work investigated on modifications of hollow fiber membranes to limit bio-fouling problems. Synthetic sea brine solutions with complex components were used in fouling experiments and the power density of PRO systems was tracked along the procedure. Zhao *et al.*[121] reported the use of MPC (2-methacryloyloxyethylphosphorylcholine)-PDA coating on PES support layer to enhance anti-fouling capacities of the system. Le *et al.*[122] presented the effect of using grated zwitterionic poly(sulfobetaine) on PA selective layers.

Table 3 lists the present work of hollow fiber PRO TFC membranes in literature.

3.1.3 Economic analysis. Ever since the appearance of PRO system, the debate on its technological and economical feasibility has never stopped. In 2008, the power density threshold for PRO commercialization was reported to be 5 W m^{-2}.[155] This result was taken as reference for the PRO application of Statkraft in Norway and for numerous studies published later. However, based on the novel economic framework developed by Chung *et al.*,[106] the economical viable threshold of PRO power density was revalued. The net power density enabling the commercial interest of PRO to compete with present solar photovoltaic power plants is estimated to be 56.4 W m^{-2}, with a suggestion of membrane cost at 15 $ per m^2. Here, the levelized cost of energy (LCOE) is set to be 0.074 $ per kW h. Net power density and gross

Table 3 A summary of present PRO systems using hollow fiber PRO TFC membranes

Materials	Concentration gradient	Hydraulic pressure (bar)	Power density ($W m^{-2}$)	Comments	Ref.
PA/PES	40 mM/1 M	9	10.6	—	110
PA/PEI	1 mM/1.0 M	15	20.9	—	111
PA/PI	DI/1.0 M	16	14	—	123
PAN-PVP/PBI-POSS	10 mM/1.0 M	7	2.5	—	135
PA/PI	DI/1.0 M	20	7.6	PDA coating	136
PA/PES	DI/1.0 M	20	24.3	—	137
PA/P84 co-polyimide	DI/1.0 M	21	12	—	115
PAN-PVP/PBI-POSS	10 mM/1.0 M	15	5.1	PAN/PVP with APS post-treatment	114
PA/PI	DI/1.0 M	15	16.5	—	138
PA/PES	DI/0.6 M	6	1.62	—	112
PA/PES	DI/0.6 M	7	3	PDA coating	113
PA/PES	DI/0.6 M	8	3.9	PA treated with TBP with PDA coating	116
PA/PES	DI/3.5% (w/w)	16	6.7	PES grafted with HPG	115
PA/PI	DI/1.0 M	16.2	12	—	139
PA/PES	DI/1.0 M	18	11.2	—	140
PBI/PVP/PAN triple layer	10 mM/1 M	22	6.2	—	141
PA/PES	DI/1.0 M	20	7.8	—	142
PA/PES	DI/1.0 M	20	22.1	Pre-stabilization	143
PA/PEI	DI/1.0 M	17	9.6	Pre-wetting	122
PA/PEI	DI/1.0 M	13	13	PA modified with APTMS	144
PA/PES	Wastewater/0.81 M	15	7.7	PES with MPC- PDA coating	121
PA/PEI	DI/1.0 M	15	19.2	—	145
PA/PEI	—	17	9.5	—	146
PA/PES	DI/1.0 M	22	10.7	—	147
PA/PES	DI/1.0 M	20	22	—	148
PA/PES	DI/1.0 M	15	10.7	PA dual layer on both sides	149
PA/PEI	DI/1.0 M	15	16.2	PA with LbL deposition of PAH and PAA	146
PA/PES	DI/0.81 M	15	11	PDA coating grafted with CQDs	118
PA/PES	DI/1.0 M	20	20	PES with $CaCl_2$ additive tuning	150
PA/PES	Wastewater/0.81 M	20	18.8	PDA coating grafted with SHPG	117
PA/PEI	DI/1.0 M	15	8.9	—	151
PA/PES	DI/1.0 M	23	34.2	PA incorporated with CDQs	119
PA/PAI	Wastewater/1.0 M	13	4.3	PAH post-treatment	152
PA/PES	DI/1.0 M	16.5	14.6	PES incorporated with GO nanosheets	120
CTA/CA T-NIPS membrane	DI/1.0 M	18	5.5	—	153
PA/PES	DI/1.0 M	17	14.6	PA incorporated with PP-SO_3H	154

power density fundamentally differ because of the inherent overhead associated with the PRO process in the form of irrecoverable pumping energy input. The importance of using net power density in PRO system characterization is emphasized for better guidance of the technology development. Several evaluations focused on different cases were also reported. Mashrafi *et al.*[156] provide an environmental and economic case study of PRO system implantation in Tampa Florida. A LCOE between 0.62–0.97 $ per kW h is estimated for feed water of different salinities. Based on the analysis model, suggestions including waste water treatment (as feed water) or PRO installation near waste water source (within 1 km) could effectively reduce the LCOE down to 0.14 $ per kW h. Khasawneh *et al.*[157] analyzed the feasibility of installing PRO power plants with Red Sea-Dead sea waters. It was demonstrated that the project is technically and economically feasible, with a LCOE of 0.056 $ and a power of 134.5 MW. The membrane cost is estimated to be 25 $ per meter square. Based on hypersaline water sources, the extractable energy density in this case study surpass the conventional river-sea water sources, providing a positive estimation on installation of PRO systems.

Straub *et al.*[78] reported a thorough energetic analysis of PRO system harvesting blue energy in river water and sea water. An estimation for energy inputs and outputs in the system was presented separately. Overall, the expected energetic inputs will most likely surpass outputs, resulting in a negative power generation. The major cause is the insufficient energy density extractable in mixing of river and sea sources. However, systems with higher concentration gradients can sufficiently overcome the energy output limit mentioned above, though technical problems including biofouling and selectivity decrease remain to be solved. Touati *et al.*[71] confirmed the viability of open-loop PRO and close-loop PRO by using low-concentration feed solutions. However, the analysis of hybrid SWRO-PRO systems results in a negative energy generation.

Though the debate of the viability of PRO system never stops, industrial attempts using PRO prototypes continues in the globe. The first commercialized plant was conducted by Statkraft in Norway from December 2009.[158] The aim of the project is to produce an 8 inch spiral wound module of 2000 m^2 which is able to produce a total of 10 kW of power, corresponding to a power density of 5 W m^{-2}.[159] However,

the actual performance of the PRO plant failed to reach the initial objective, delivering a total power of 2 kW, which corresponds only to 20% of the designed power.[160] Due to the lack of membrane optimization and high cost in accessory systems, the sale price of a PRO plant reaches 70–100 euros per MW h and showed low economic interests, compared with the actual electricity price of 30–40 euros in Norway. The whole system was unfortunately shut down in 2013. Researchers and engineers performed another prototype experiment in Quebec, Canada.[159] The main objective of the project is to carry out process optimization studies of performing water pretreatment to prevent biofouling problems. A novel project was started in Japan to install an additional prototype PRO module, using commercial CTA hollow fiber membrane modules, to the Fukuoka WRO desalination plant to form a RO-PRO joint system.[159] A maximum power density of 13.3 W m^{-2} was achieved by a 10 inch hollow fiber membrane module. Nowadays, a similar hybrid RO-PRO project is developed jointly by Saudi Arabia and Japan, aiming to develop efficient PRO systems for energy recovery and environmentally friendly high saline water treatment used in RO desalination processes.[161]

Overall, stand-alone PRO systems with sources of higher salinity difference seem to be more promising due to a higher extractable energy density. The development of commercialized inexpensive PRO membranes is of key importance, which could sufficiently increase the system performances and reduce the production and maintenance costs. Considering the rising electricity price in Europe due to the lack of gas and the emerging technology development in PRO systems, the economic threshold of PRO system might be reached in the near future.

3.2 Reverse electrodialysis

Proposed by Pattle *et al.* in 1954,[162] reverse electrodialysis (RED) is the earliest technology proposed for blue energy extraction. In a classic RED configuration, sea water and river water were injected respectively into two different compartments separated by an ionic exchange membrane (IEM). This approach corresponds to the reversed process of the electrolysis (ED), where IEMs are used with an electric current to remove salts from sea water for pure water production. Years after, no significant development has done until 70s, when Lacey in 1980 developed his model for the RED.[163] To understand how an RED device works, it is necessary to understand how an ion exchange membrane behaves when it separates two salt solutions of different concentrations. This question will be answered in the following subsection.

3.2.1 An ionic exchange membrane separating two different salted solutions. An electrical potential difference occurs between two solutions of different salinity when an ion exchange membrane separates them. As illustrated in Fig. 13,

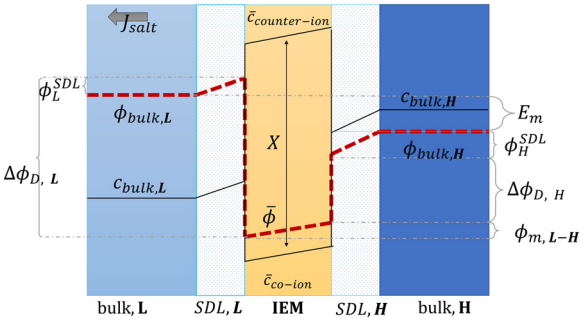

Fig. 13 Schematic representation of concentration, c, and potential, ϕ, profile in the bulk solutions, the stagnant diffusion layers (SDLs), and in an ion exchange membrane (IEM) (figures and captions adapted from ref. 164 with permission from FIMTEC & MPRL, copyright 2016).

this potential difference is the sum of several terms[164] and writes: $E_m = \Delta\phi_{D,L} - \Delta\phi_{D,H} + \phi_{m,L-H} + \phi_L^{SDL} + \phi_H^{SDL}$.

$\Delta\phi_{D,L}$ is called the Donnan potential in the diluted solution. It comes from the difference in ion concentration at the solution–membrane interface. In this context, the equality of chemical potentials leads to:

$$\mu_i^0 + RT\ln(a_{i,L}) + z_i F\phi_L = \mu_i^0 + RT\ln(\bar{a}_{i,L}) + z_i F\bar{\phi}_L \quad (4)$$

$$\Delta\phi_{D,L} = \frac{RT}{z_i F}\ln\left(\frac{\bar{a}_{i,L}}{a_{i,L}}\right) \quad (5)$$

where F is the Faraday constant, z_i the valence of the ion, R the gas constant, T the temperature, $a_{i,L}$ and $\bar{a}_{i,L}$ are the activity of the ions on the external and the internal side of the membrane in the diluted electrolyte, respectively. ϕ_L and $\bar{\phi}_L$ are the electrical potential on the external and the internal side of the membrane in the diluted electrolyte, respectively. $\Delta\phi_{D,H}$ is the Donnan potential characterizing the concentrated solution. $\phi_{m,L-H}$ is the difference of potential occurring inside the membrane. ϕ_L^{SDL} and ϕ_H^{SDL} are the difference of potential created by stagnant double layers (boundary layer) that build up close to the membrane. These layers, also named as polarization layers, have fundamental impacts with the presence of electric current. As we will see later, they are usually considered as non-ohmic resistances in the analysis of RED systems. The modeling of all these terms is complex and requires complicated numerical simulations.

A simple limit can be found. In the absence of electric current through the membrane, in the case of a rigorously selective membrane, the diffusion potential vanishes. Neglecting the stagnant double layers, the open circuit voltage writes:

$$E_m = \frac{RT}{z_i F}\ln\left(\frac{\gamma_H c_H}{\gamma_L c_L}\right) \quad (6)$$

where γ_H and γ_L the activity coefficients, and c_H and c_L are the concentrations of concentrated and diluted respectively, with $a_i = \gamma_i c_i$.

Under the assumption of an open circuit and neglecting the polarization layers, this equation can be generalized to a non-selective membrane by writing: $E_m = \alpha \frac{RT}{z_i F} \ln\left(\frac{\gamma_H c_H}{\gamma_L c_L}\right)$, where $\alpha = \frac{t^+ - t^-}{t^+ + t^-}$ with t^+ the transport number of the cation and t^- the transport number if the anion. To go further and calculate α, the modeling of all these terms is required. The most widely used description comes from the Teorell–Meyer–Sievers[165] theory which is a one-dimensional model that does not take into account the ions concentrations variations in the pore section of the membrane, nor the fluid transport by convection. The space charged model developed by Osterle and colleagues[166] takes into account these two points. Recently, interactions with surfaces and electro-osmotic effects have been taken into account in calculations to explain the strong ionic currents generated by charged but *a priori* non-selective nanotubes of more than 20 nanometers in diameter.[167] We will return to this point later in the text.

In a more pragmatic way, this description of the membrane potentials leads to propose an electrical scheme for a membrane. In the presence of different salt concentrations on both sides of the membrane, the membrane behaves like a voltage generator E_{OCV} which is the open circuit voltage in series with a resistor and with elements that account for the polarization layers. These double layers are resistors in parallel with phase elements or simply resistors.[168,169]

3.2.2 The RED cell. The RED device takes advantage of the potential difference that appears on an ion exchange membrane when it separates two saline solutions of different concentrations. A classic RED stack configuration is illustrated in Fig. 14. Two types of IEMs are used in this configuration: anionic exchange membranes (AEMs) which allow the passage of anions and cationic exchange membranes (CEMs) which allow the passage of cations. These membranes are separated by spacers and are placed alternatively so as to form alternative water compartments. Diluted and concentrated solutions are injected continuously in water compartments by pumps. At two ends of the stack, two electrodes are placed with circulating electrolytes for energy conversion by redox reactions. In each compartment of the cell, where the solutions can circulate generally through a spacer to ensure an uniform flow, the ions try to move from the concentrated solution to the dilute solution to balance the chemical potentials, but due to the charge of the IEMs, only one type of ion is allowed to pass and the other type will be rejected. Thus, an ionic flux is generated allowing an electrochemical potential to establish in the surface of the membrane called Donnan potential. This potential is converted to electricity by faradaic reactions at the end of the cell by the electrodes and electrolytes.

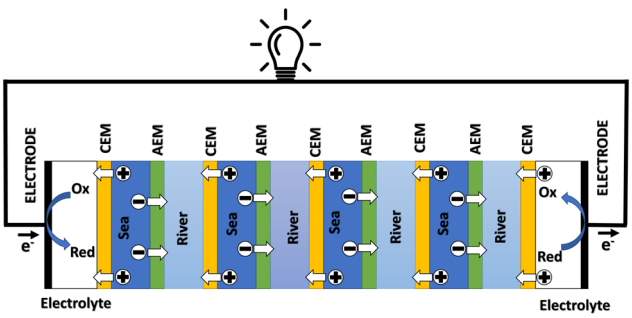

Fig. 14 A schematic illustration of the RED process.

In the following we will detail all the elements of the cell.

Electrodes. Electrodes are used in RED stacks for the conversion of osmotic-driven ionic flux into an electric current by faradaic reactions. The choice of electrodes is of great importance for the optimization of energy conversion efficiency in RED stacks.[170] Several electrodes were proposed for RED systems, from participating electrodes like Ag/AgCl to inert ones like Pt, and with redox reactions ranging from hydrogen/oxygen reactions to more complex like $Fe(CN)_6^{3-}$/$Fe(CN)_6^{4-}$. These electrodes are classified to three main types summarized in the Table 4. The oldest electrodes[162,171] were made of two metals immersed in a solution containing the metal ions. The metal (or the amalgam such as Ag/AgCl) participates directly in the red-ox reaction. Thereby, the electrodes were consumed during the process and their life span remains limited. For theses reasons, participating electrodes were dropped out in the latest development.[172,173] After that, inert electrodes were proposed to avoid the regeneration problem. They interact directly with the electrolytes and forming gases which is their major drawback.[174] Inert electrodes are used jointly with redox couples dissolved in the circulating electrolytes to enable the redox reactions for energy conversion. Inert electrodes present enormous applications in RED systems due to good chemical/environmental advantage. The consumed ions in one electrode will be generated in the other one, and thus leading to no net chemical reaction at the end. In the same time, because of this, the electrolyte will be conserved and no over-potential will be appear because of the gas formation. The problem with this category is the nature of the couple: for the $FeCl_2/FeCl_3$ system, low pH is needed to prevent formation of solid (hydr)oxides[172] and for the Fe-complex couple, it is not stable during long time especially if exposed to light.[175]

Ionic exchange membrane. The RED is a membrane based osmotic process where IEMs are considered as the main engine of the energy recovery. Membranes are usually characterized by several properties based on the amount, structure, type and the charge of the functional groups in the membrane. These proprieties are linked. IEMs are divided to three main classes: CEMs, AEMs and bipolar membranes according to the surface charge. CEMs possess negative charges with a fixed chemical group. Generally, chemical groups of strong acids, like sulphonate ($-SO_3^-$) and phosphorate ($-PO_3^-$), or weak acids like carboxyl groups ($-COO^-$) are used in CEMs. Due to the presence of negative charges in CEMs, anions in solutions are repulsed and the

Table 4 A summary of electrodes used in the RED

Type	Electrodes	Electrolyte	Advantage	Disadvantage	Ref.
Inert electrodes with reversible reactions	Ti–Ru/Ir mesh	$K_4Fe(CN)_6$ $K_3Fe(CN)_6$	No electrolysis voltage losses	Sensible to light	176
	Ti–Ru/Ir mesh	$Fe(Cl)_2/Fe(Cl)_2$	No net chemical reaction Bidirectional system	Sensible to pH	172
Inert electrodes with irreversible reactions	Ti-Ru/Ir mesh	NaCl	No net chemical reaction	Voltage loss H_2 generation	174
	Ti–Pt mesh	Na_2SO_4		Cl_2 generation	177
Participating electrodes	Ag/AgCl	NaCl	No net chemical reaction	Switching flows	178
	Cu	$CuSO_4$	No electrolysis voltage losses	Electrodes regeneration	162
	Zn	$ZnSO_4$			171

Table 5 A summary of the most used IEMs in literature

Membrane	Thickness (μm)	IEC (meq g^{-1})	SD (%)	CD (meq g^{-1} H_2O)	α (%)	R (Ω cm^2)	Ref.
CEM							
Neosepta CMX	164	1.62	18	9.0	99	2.91	179
Neosepta CMS	150	—	—	—	97	1.4–1.8	180
Neosepta CM-1	133	2.3	20	11.5	97.2	1.67	179
Neosepta CIMS	150	2.3	30	7.7	—	2.49	181
Fumasep FKD	113	1.14	29	3.9	89.5	2.14	179
Fumasep FKS-20	20	1.24	—		99	1.7	182
Fumasep FKE	34	1.36	12	11.3	98.6	2.46	179
Selemion CSO	—	1.04	16	6.4	92.3	2.26	183
Selemion CMV	101	2.01	20	10.1	98.8	2.29	179
Fujifilm V1	125	—	—	—	93	1.6	184
Fujifilm CEM RP1 80050-04	120	1.45	—	—	96	2.55	182
Nafion-115	139	0.9	—	8	—	—	185
Nafion-117	201	0.9	—	7.7	—	—	185
Ralex CMH	764	2.34	31	7.5	94.7	11.33	179
Qianqiu CEM	205	1.21	33	3.7	82	1.97	186
Tailor-made SPEEK 65	72	1.76	35.6	—	89.1	1.22	186
Tailor-made SPEEK 40	53	1.23	23	—	95.3	2.05	186
AEM							
Neosepta AM-1	126	1.77	19	9.3	91.8	1.84	179
Neosepta AFN	163	3.02	43	7	88.9	0.7	179
Neosepta AMX	134	1.25	16	7.8	90.7	2.35	179
Neosepta ACS-8T	150	1.9	—	—	—	2.41	181
Fumasep fad	74	0.13	34	0.4	86	0.89	179
Fumasep fas-20	20	1.5	31.25	4.8	95.5	0.5	182
Selemion DSV	121	1.89	1.03	183.5	89.9	1.03	179
Selemion APS	138	0.29	147	0.2	88.4	0.68	179
Selemion AMV	110	2.2	21	10.5	95	2.44	187
Fujifilm TYPE I	115	—	—	—	91.9	1.3	180
Fujifilm AEM RP1 80045-01	120	1.28	—	—	96	1.83	182
Fujifilm V3B	84	1.7	23	7.39	87	1.36	187
Fuji V3A	66	2.2	23	9.57	82	0.87	187
Fujifilm V1	139	1.8	23	7.83	90	1.05	187
Fujifilm V2	53	1.6	23	6.96	86	0.67	187
Ralex AMH-PES	714	1.97	56	3.5	89.3	7.66	179
Qianqiu AEM	294	1.33	35	3.8	86.3	2.85	186
Tailor-made PECH A	77	1.31	32.2	4.1	90.3	2.05	186
Tailor-made PECH B2	77	1.68	49	3.4	87.2	0.94	186
Tailor-made PECH B1	33	1.68	49	3.4	86.5	0.82	186

cations pass. For AEMs, cations are repulsed due to the positively charged chemical groups including ammonium ($-NR_3^+$), primary amine ($-NH_2$), secondary amine (–NRH) and tertiary amine ($-NR_2$). Bipolar membranes have simultaneously negative and positive chemical groups and display fascinating applications in water splitting. The main characteristics of commercial membranes, *i.e.* the swelling degree, the ion exchange capacity, the fixed charge density, the permselectivity, and the membrane resistance are reported in the Table 5.

The swelling degree (SD) characterizes the ability of a dry membrane to absorb water. It measures the mass change ratio of a dry membrane before and after water immersion:

$$SD = \frac{m_{wet} - m_{dry}}{m_{dry}} \times 100 \quad (7)$$

where m_{wet} is weight of the wet IEM and m_{dry} is weight of membrane in its dry phase.

Ion exchange capacity (IEC) determines the number of fixed charges inside the IEM per unit of mass of a dry membrane. The fixed charges in the membrane are usually in equilibrium with the ions in the electrolytes, this equilibrium is given by the Fixed charge density (CD) and it is defined as the milliequivalents of charged groups per gram of water in the membrane. It is given by:

$$CD = \frac{IEC}{SD} \quad (8)$$

The permselectivity (α) is one of the most important parameters for ionic exchange membranes. It describes the ability of a membrane to reject co-ions (ions of same charge) and allow the passage of counter ions. An ideal membrane, which blocks all co-ions and allows passage of 100% of counter ions, is characterized by a selectivity of 1. In practical applications, the effective selectivity can be calculated by the ratio between the electrical potential measured between the electrodes and the theoretical one for an ideal membrane under a given gradient.

The membrane is a part of an electrochemical cell where the ionic current is converted to an electrical one. This current is directly affected by the conductivity of this membrane (ohm loss) and can influence the power density. This resistance is reported to a unit of area. It depends on the material's property and its structure (see Table 5).

These properties depend on the conditions of use such as the concentrations of the saline solutions, the value of the difference in salinity, the acidity, the temperature. Using a very high concentration can reduce membrane selectivity even though it gives better conductivity.[169,173] A high temperature[173] decreases the permselectivity of the membrane.

The characteristics of the membranes depend on the mode of production based on which IEMs are classified into homogeneous IEMs and heterogeneous IEMs.

For the first class, the membrane is prepared using just one product, generally, by polymerization of a charged/can be charged monomers or followed by grafting functional monomers on a film/dissolved polymer.[188] On the other hand, heterogeneous IEMs contain two parts, an ionic exchange resin mixed with an uncharged polymer matrix without any chemical bound. Homogeneous IEMs exhibit excellent electrochemical properties, very low resistances and high permselectivity.[189] Their thickness is between 1 and 30 μm. However, their production is more complicated and more expensive. In contrast, heterogeneous IEMs are easier and less expensive to prepare with a good mechanical and chemical stability especially for the AEMs in alkaline electrolyte. However, their high resistance is still a major challenge for the RED technology.[179] Recently, N. D. Pismenskaya *et al.*[189] modified an heterogeneous membrane by grafting functional quaternary ammonium groups to increase its electrochemical performance. The results are encouraging and close to that of a homogeneous IEM.

3.2.3 The power density. The maximal electrical power density in a RED cell is given by[174]

$$P_{max} = \frac{{E_{ocv}}^2}{4R_{cell}} \quad (9)$$

where E_{ocv} is the potential generated using an ionic exchange membrane between two solutions under a salinity gradient. It can be described by the following equation:

$$E_{ocv} = \alpha N \frac{RT}{zF} \ln\left(\frac{c_H \gamma_H}{c_L \gamma_L}\right) \quad (10)$$

With α the selectivity of one membrane, N the numbers of membranes, T the temperature, z the valence (z = 1 for Na^+), R the gas constant, F the Faraday constant, γ_H and γ_L the activity coefficients, and c_H and c_L are the concentrations of concentrated and diluted solutions, respectively. And R_{cell} is the cell resistance which consists of two main parts, an ohmic one that represents the conductivity of cell components (including membrane, solutions, spacers, and *etc.*) and a non-ohmic part which involves the concentration change inside the cell. The non-ohmic part is caused by the polarization effect near membranes and by the salt concentration variation along the water channel.

To develop a production cell, it is necessary to choose the number of membranes to be used. *A priori*, it is interesting to increase the number of membranes. Using a large number of membranes should make the whole device more compact. When the salinity of the solutions is fixed, E_{ocv}, and P_{max} increases theoretically linearly with the number of cell pairs and is independent of the flow rate. The power density should therefore not be depend upon the number of membranes.

Experimentally, H. Kim *et al.*[196] observe a different behavior. When the stack is supplied with a constant flow, the gross and net power density decrease when the number of membranes becomes higher than.[200] These phenomena are caused by the polarization of the cell. When the pairs of cells are more numerous, the local flow rate decreases in each cell which favors mixing, the appearance of a concentration gradient along the flow and the growth of the thickness of stagnant ionic layers.

In fact it comes from the polarization the open circuit potential increases with the number of cell pairs but the growth law between the two is weaker than a linear law. When the number of cells is fixed, the open circuit potential increases slightly with the flow rate. As the number of cells increases, the throughput in each cell is lower and the polarization effects along the cell but also the thickness of the depleted layers increases. Both effects induce a decrease of the open potential.

According to eqn (9), an efficient way for power density optimization is to increase the open-circuit voltage E_{ocv}.

Several research works managed to ameliorate the membrane selectivity a or increase the number of IEM pairs used in RED systems. Güler *et al.*[186] tested several IEMs and found that the permselectivity could be independent of the thickness. H. Kim *et al.*[196] showed that the using a big number of cell pair will affect the residence time of the ions inside and therefore the concentration polarization inside the cell will cause a diminishing of the potential compared to the theoretical value.

For the non-ohmic resistance, the challenge is always present. Vermaas *et al.*[193] attempted to improve mixing inside the cell to reduce the boundary layer using a specific spacer with filled channels and with sub-corrugations (see Fig. 15B) without much success.

Though the use of more than 45 membranes in the RED system, Pattle *et al.*[162] reported a mild power density of 0.2 W m^{-2} because of the low efficiency of their stack. Numerous studies continues today in the hope of promoting output power density of RED systems. In 2007, Dlugolecki *et al.*[179] investigated the performance of several membranes used generally in the RED, and estimated that a power density of 6 W m^{-2} can be achieved by commercial IEMs. A year after, a power density of 0.84 W per square metre of membrane was obtained in the work of Turek *et al.*[177] with a high salinity gradient (around 200) and even a 0.9 W m^{-2} is reached by Veerman *et al.*[190] with a salinity difference of 30 g L^{-1} *vs.* 1 g L^{-1} of NaCl for the concentrated and the diluted solution respectively. High cell resistance hinders the electrical performance of RED systems.[174] It was reported that the diminution of spacer thickness (from 485 μm to 100 μm) could effectively reduce the ohmic resistance of the system by 4.[176] With these RED improvements, Vermaas *et al.*[176] obtained a gross power density of 1.8 W m^{-2} using just 5 pairs of IEMs. However, for thinner spacers, a higher pressure loss was reported. A net power density of 1.2 W m^{-2}, which remains the highest experimental net power density documented until present, was achieved in this work. The same team tried to removed the spacers and employed profiled membranes to reduce water volume (higher conductivity). While a significant ohmic resistance drop of 30% was achieved, the profiled membranes suffered from severe polarization problems which reduces the ohmic resistance around 30% but the polarization resistance was significantly higher.[191] Adding sub-corrugations to disturb the uniform flow and enhance the mixing was insufficient to increase the net energy power.[193]

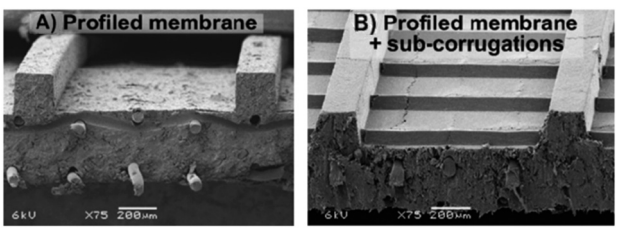

Fig. 15 Images obtained from a scanning electron microscope for (A) the profiled membranes (B) and profiled membranes with sub-corrugations (figures and captions reproduced from ref. 193 with permission from Elsevier, copyright 2014).

As already described, the potential E_{ocv} between the stack's electrodes is directly related to the gradient. Daniilidis *et al.*[173] investigated the RED stack for hypersaline solution like the Dead sea, with a concentration close to the saturation (around 5 M) with a river water of 0.01 M concentration and they obtained a gross power density 3.8 W m^{-2} at 25 °C and more than 6.5 W m^{-2} at 60 °C in 5 membrane pairs cell, even if the selectivity was lower with the increasing of the temperature and the gradient. This power density corresponds to a gross power. It's worth to note that even though this energy was experimentally measured, no pumping energy consumption was subtracted. In the same topic, and to show the effect of temperature and gradient, Tedesco *et al.*[182] used a hypersaline solution at 5 M and a brackish solution with 0.1 M, and reached a gross power of 6 W m^{-2} at 40 °C in a cell with 50 membrane pairs. In this situation, the resistance of membrane pairs is low.

In fact, the recorded experimental gross power density without correction was around 4.75 W m^{-2} with 2–2.5 W m^{-2} of dissipated power due to the pressure drop inside the cell. Increasing the unit size to the double and the number of the membrane pairs had only a slight reduction in the power density caused by the non-uniform distribution of fluids concentration. The amount of the theoretical power is very huge, it is estimated to be more than 2 TW in the world rivers and oceans.[8] Just a part of this power is actually exploitable by the blue energy harvesting technologies. The efficiency is defined as the ratio between the recoverable energy and the available Gibbs free energy in the water mixing of unit volume. Higher energy efficiency is achieved when the feed waters are recycled (multiple pass)[176] and a lower current density is applied (due to ionic shortcut currents).[190]

$$\eta = \frac{P_{max} \cdot A}{\Delta G_{mix} \cdot Q} \tag{11}$$

where A is the membrane area and Q the flow rate. For the RED process, it depends on the flow rate and on the capacity of the membrane to exchange ions. As represented in the Table 6, the efficiency remains under 50%.

3.2.4 Nano RED. One way to increase the collected current density is to decrease the cell resistance and thus the membrane resistance. To do this, it has been proposed to work with membranes with nanometric sized holes. This attractive idea is based on the initial work on single nanotube. Remarkably, a giant ionic current was measured when a non-selective boron nitride nanotube (BNNT) is placed in a salt gradient (see Fig. 16).

For a BNNT placed between a 1 M and 0.01 M NaCl solution the authors measure[167] an electric current of 1 nA and a power density of 4 kW m^{-2} for a nanotube (see Fig. 17). This point is very remarkable. This potential is created by an

Table 6 The summary of processes of RED reviewed literature

Membrane	C_H (M)	C_L (M)	Temperature (°C)	Power density (W m^2)	Efficiency	Ref.
Fumasep FKD/FAD	0.507	0.017	25	0.93	18%	190
Neosepta CMX/AMX	1.899	0.01	—	0.72	—	177
Fumasep FKS/FAS	0.507	0.017	25	2	32%	176
Fumasep FKS/FAS	0.507	0.017	25	1.8	15%	176
Ralex Profiled CMH/AMH	0.507	0.017	25	0.8	<1%	191
Tailor-made SPEEK65/PECH B2	0.513	0.017	25	1.28	—	192
Qianqiu CEM/AEM	0.513	0.017	25	0.83	—	192
Custom-made composite/Selemion CEM/ASV	0.5	0.017	25	1.3	—	183
Ralex Profiled + sub-corrugations CMH/AMH	0.507	0.017	—	0.9	—	193
Neosepta CMS/ACS	5	0.01	25	3.8	7%	173
Neosepta CMS/ACS	5	0.01	60	6.7	20%	173
Fumasep FK-20/FAS-20	5	0.1	40	4.75	<1%	182
Fujifilm CEM 80045-04/AEM 80045-01	4–5	0.03	23	1.35	2–3%	194
Fujifilm CEM-80050/AEM-80045	0.762	0.005	20	0.3	—	195
Fujifilm CEM-80050/AEM-80045	0.762	0.005	60	0.705	—	195
Nafion/Neosepta N117/AMX	4	0.5	25	1.38	—	185

electrophoretic flux due to the surface charge of the nanotube. Boron Nitride surfaces bear a large surface charge.

The ion concentration profile of the salt solution placed above this surface is given by: $C_{\pm}(x,z) = C_{\infty}(x)\exp^{(-\pm\phi(z))}$ where $\phi(z)$ is the electrical potential, z the vertical position normal to the surface, x the position along the direction of the surface, $C_{\infty}(x)$ the concentration in salt far from the surface, $C_{+}(x,z)$ the concentration in positive counterions, $C_{-}(x,z)$ the concentration in negative counterions as a function of x and z. The balance along the z direction between the pressure forces acting on a fluid particle and the electrostatic forces links the pressure and concentration fields. This writes: $P(x,z) = P_{\infty} + 2k_BTC_{\infty}(x)\cosh(\phi(z) - 1)$ the concentration gradient along the loaded surface induces thus a pressure gradient

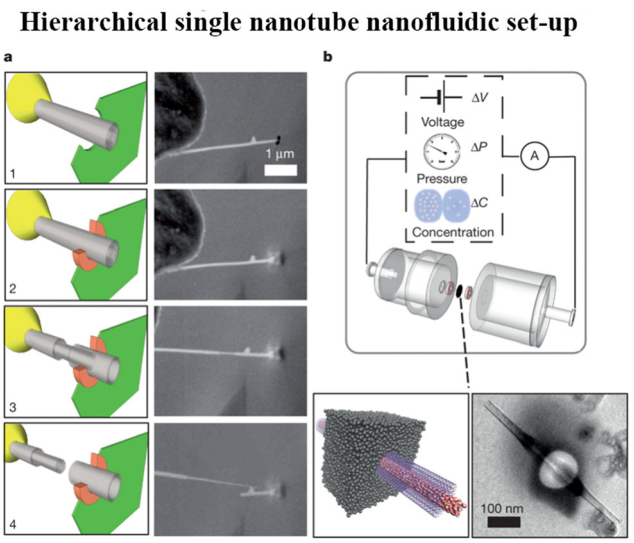

Fig. 16 a, *In situ* nanomanipulation of a BNNT (left, sketch; right, scanning electron microscope (SEM) images): 1, insertion of a BNNT (grey) through a nanopore drilled in a SiN membrane (green) using a focused ion beam (FIB); 2, carbon sealing of the FIB-drilled hole using local electron-beam-induced deposition (orange); 3, telescopic retraction of internal walls of the BNNT; 4, finalized transmembrane BNNT device. b, Top, Schematic of the experimental set-up for measuring fluid transport through the single BNNT. Bottom, sketch of the final transmembrane BNNT for nanofluidic measurements (left) and its experimental realization, imaged by transmission electron microscopy (TEM) (right) (figures and captions reproduced from ref. 167 with permission from Springer Nature copyright 2013).

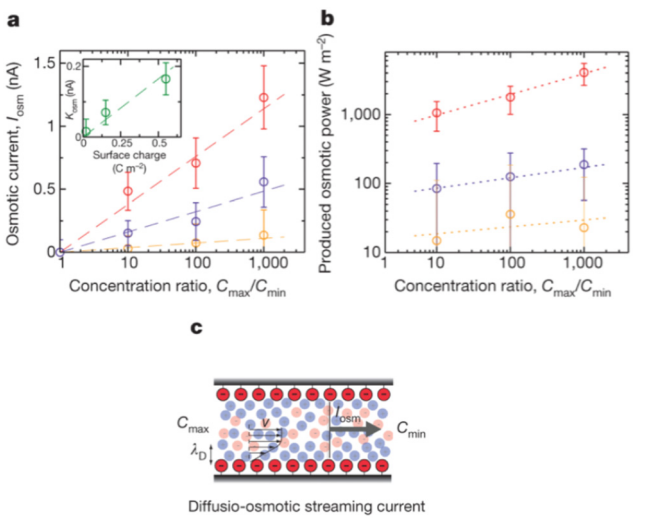

Fig. 17 a, Osmotic streaming current *versus* concentration difference for a t-BNNT with R, L 5 40 nm, 1250 nm and pH 5.5 (yellow), 9.5 (purple) and 11 (red). The experimental points show measurements for various salt concentrations in the two reservoirs, with C_{min} and C_{max} in the range 10^{-3}–1 M. Error bars follow from the corresponding error analysis. Dashed lines are linear fits: $I_{osm} \propto \log\frac{C_{max}}{C_{min}}$. Inset, Osmotic mobility *versus* surface charge. Surface charge is obtained from independent conductance measurements. The dashed line is a linear fit with proportionality factor of 0.33 for the chosen units. b, Corresponding power density (per unit surface of the BNNT) for the three values of pH. Dotted lines are a guide to the eye. In the present graph, the minimum concentration is fixed to $C_{min} = 10^{-3}$ M. b, Sketch of the osmotically driven streaming current under a salt concentration difference, $C_{max} - C_{min}$ (figures and captions reproduced from ref. 167 with permission from Springer Nature, copyright 2013).

along the same surface. This pressure gradient is at the origin of a Stokes flow in the nanotube whose maximum speed is given by: $V = \frac{k_B T}{2\pi\eta l_b} \ln(1-\gamma^2) \frac{d \log C_\infty}{dx}$ with $\gamma = \tanh\left(\frac{e\phi_o}{4k_B T}\right)$ and ϕ_o the surface potential. The diffusion–osmotic flow drags the ions and produce an electric current by convection of the ions in excess. We recall that as the surface is charged, and as the liquid plus the surface is neutral, the liquid alone bears a charge which is opposed to the surface one. The obtained electrical current and potential drop are proportional to $\Delta \log C_\infty$. This modeling is in quantitative agreement with the measurements.

A quantitative analysis of these equations shows that the power gain in the system comes from the very low electrical resistance of the nanopores. The potential difference across the nanotube is not exacerbated and remains about 100 millivolts under classic experimental conditions. The theory recovers an expression close to the one presented for the selective membrane when the radius of the nanopore goes to zero and when the surface charge is high. This study has prompted many groups to prepare membranes with nanopores to increase the performance of the RED. At this stage, all the attempts end in failure to create large-scale membranes. Fig. 18 compares the power and extrapolated on 1 m^2 surfaces and the powers measured on membranes. Clearly there is no correspondence between the two and the maximum powers obtained remain below 10 W m^{-2}. This results comes from the existence of collective effects between nano-channels that prevent the generalization and extrapolation of the results obtained on a single nanotube.

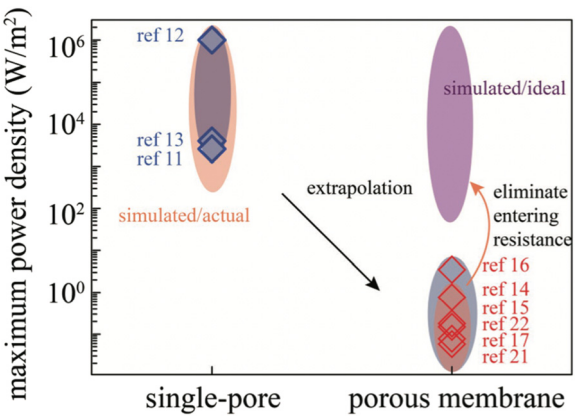

Fig. 18 Comparison between literatures reported power density and our simulated results. The range of simulated actual power density (upper left and lower right orange ovals) is approximately in agreement with that reported by literatures (blue diamond represents reported values) for both single-pore and nanoporous membrane systems, suggesting that our intuitive resistance paradigm semiquantitatively explains the orders- of magnitude power density gap between single-pore and nanoporous membrane systems. Remarkably, by eliminating the entering resistance, the simulated ideal power density (upper right oval) of membrane materials can be brought back to the single-pore level (figures and captions reproduced from ref. 197 with permission from John Wiley and Sons, copyright 2019).

When the nanotubes are too close together in the membrane, the formation of ion depletion layer results in an effective concentration difference much smaller than the imposed one. The transport of an electrolyte within a single nanotube is therefore very different from that within a membrane.[197] The results obtained, although disappointing at the level of extrapolation, are nevertheless better than the powers obtained in the experiments with polymeric membranes. It is necessary to comment on this point. All the experiments conducted on large hole membranes are done on systems with very small surfaces generally smaller than 0.01 mm^2. The system that allows the measurement of powers includes large volume of electrolyte and electrodes of large size. In this case the ionic resistance of the compartments is negligible compared to the resistance of the membrane, which is absolutely not the case in the RED experiments.

It is therefore impossible to compare these data to the RED experiments. Liu *et al.*[198] have developed a nanoporous carbon membrane *via* the thermal crossing of polycyclic aromatic hydrocarbons. They obtained a mechanically robust membrane of size 1 cm with 3.6 ± 1.8 nm pores and a thickness of 2.0 ± 0.5 nm. The pore density is close to 10^{10} pore by cm^2. They carry out RED experiments on a membrane 1 micrometer in diameter. They obtain by mixing artificial seawater (0.5 M NaCl) and river water (0.01 M NaCl) a power density of 67 W m^{-2} for a circuit resistance of 15 MW. In the context of the experiment, the dominant resistance corresponds to the resistance of the membrane. The resistance of the electrolyte compartments is negligible. The resistance of the membrane can therefore be calculated and estimated to 0.19 Ω cm^2. This figure takes into account the resistance of the membrane and the resistance of the double layer near the membrane. It forgets the ohmic resistance of the solutions and the polarization resistance due to the drop of the concentration gradient along the membrane. Note that the values reported on Table 5 are closed to this one even though they do not take into account the resistance of the double layer near the membrane. To conduct a fair comparison, calculations of magnitude's order are necessary. The power generated by this membrane in the nanofluidic system is 67 W m^{-2}. To generate such power, a flow rate equal to $Q = \frac{P}{\Delta G_{mix}} = 4.7 \times 10^{-5}$ m^3 s^{-1} is required assuming an efficiency of 100%. This corresponds to a viscous power by unit area of $P_{vis} = \frac{12\eta Q^2}{e^3 b^2}$ of 26 MW m^{-2} for a gap e of 1 μm and 26 W m^{-2} for a gap e of 100 μm. The ohmic resistance of a 0.01 M saline solution is equal to 7.8 Ω cm^2 for a gap e equals to 100 μm. This value is much higher than the resistance of the membrane and must be added to it to calculate the performance in a device of 1 square meter. Clearly it will therefore be impossible to achieve such high performance in a device of one square meter in area. It is not possible to compare the power from nanofluidic devices and centifluidic devices with conventional membranes. An interesting study would be to measure the resistance of

classical ion exchange membranes such as Nafion in nanofluidic systems.

In the previous framework, the creation of an ionic current in nanopores of several nanometers in diameter comes from the surface charge. Another way to do this is to be inspired by nature by creating nanopores covered by a very thin selective membrane. The realization[199] of robust mushroom-shaped (with stem and cap) nanochannel array membrane with an ultrathin selective layer and ultrahigh pore density, has notably allowed to obtain a power of 15 W m^{-2} with a 10 mM/0.5 M salt gradient. The experiments are performed on a membrane of 8000 μm^2. From the data of the article, it is possible to calculate the resistance of the membrane. This resistance is 1.6 Ω cm^2. As discussed previously, such feature is very close to the one of classical membranes, which is unlikely to present exceeded performances in our point of view.

3.2.5 River and sea water salted solutions. In order to demonstrate the feasibility of the RED approach, complex salt components, including various multi-valence ions, are added into concentrated and diluted solutions to simulate natural solutions in RED systems. Vermaas *et al.*[184] have investigated the influence of multivalent ions on the performance of cell with several membranes and different compositions for the feed solutions. The power density has a drop up to 50% for certain IEMs with the mixing of 10% $MgSO_4$ to the NaCl, and thus because of the uphill transport described in ref. 200. In fact, the valence of divalent ions is the double compared to the monovalent one, create a lower open circuit voltage. But also, the resistance is more important because of the lower diffusion coefficients of multivalent ions compared to Na^+ and Cl^- with a strongest steric hindrance of Mg^{2+}, Ca^{2+} relative to Na^+.[184] The same effect was noticed by Tufa *et al.*[201] when they added Mg^{2+} to the feed: a 64% loss of maximum power was reported. In addition, when they tested imitating real brackish water and exhaust brine with several ions, they got 63% loss in power density.

To overcome this problem, monovalent ion exchange membranes were proposed to replace the usual IEMs. Guler *et al.*[192] compared two commercial monovalent AEMs with a home-modified one, and they found that there is no significant difference on the measured gross power densities between the monovalent and the multivalent IEMs because of their high internal resistance.[180,192] Moreno *et al.*[180] tried two different strategies to minimise the negative effect of uphill transport (multivalent ions transport against the concentration gradient). The first one is using a highly cross-linked cationic monovalent membrane. This type of IEMs select the ions with the same charge based on their size (hydrated ionic radius). It blocks the multivalent ions and allows the transport of monovalent ions only. The second strategy is based on the charge rejection. A standard CEM with a thin positively charged layer on the membrane surface. A constant OCV was obtained using a mixing between NaCl and $MgCl_2$ compared to pure NaCl solution for the monovalent CEM. Also, for the coated CEM, a slight decrease in the OCV was observed. The membrane resistance was higher due to the lower ion mobility of magnesium ions inside these membranes. Hence, the power density was lower.

3.2.6 Fouling. The natural solutions are even more complicated and contain more species than the ions. Several works studied the behavior of RED stacks with natural feed. Kingsbury *et al.*[202] evaluated the response of a RED unit fed with five different pairs of real waters and wastewaters. They reported that natural organic matters reduced power densities by up to 43%. Cosenza *et al.*[203] tested different solutions from oil industrial wells, where the high concentrated solution contains an important amount of organic and dissolved solids, and the diluted solution was prepared with 0.7 g L^{-1} NaCl solution. They measured a greater resistance (around 40% at less concentrated solution) for the natural one compared to a NaCl-artificial salt water causing a 17% power loss. That effect was even worse when natural solutions from Licetto River and Tyrrhenian Sea in Italy were used in concentrated and diluted compartments, respectively.[195]

In addition to this negative effect, fouling remains a tricky problem in long-term experiment, causing severe resistance increase and permselectivity hindrance. In 2012, Vermaas *et al.*[204] established RED stacks with water feeds of naturel river water (Van Harinxmakanaal – Netherland) and natural sea water (Wadden Sea – Netherland) filtered by a 20 μm diameter filter. During the 25 day continuous test, they observed a significant resistance rise, along with a slight decrease in membrane permselectivity, which results in a power loss of 60% of the RED system. This result was confirmed by the work of Vital *et al.*,[205] where after 54 days, the power density decrease by 25%. This fouling comes in two major parts of the RED stack, the IEMS and the spacers. For the IEM we can determine two kinds of fouling depending on the charge of the membrane: the organic and the bio-fouling, generally negatively charged, are more occurred on the AEMs. In contract of the CEM, where the main problem is scaling and the solid particles. In the other hand, the fouling in the spacer can directly detect by a drop pressure jump inside the cell[204] and channel clogging, shown by Cosenza *et al.*,[203] due to bacteria growing in the channels of the RED unit and in the dilute solution circuit, hence, The fouling is most probably in river water.

To control this fouling, various strategies are proposed at different levels: before pumping the steams, inside the RED stack, by slowing the formation of fouling and after by removing all blocking particles.

The first barrier can be a simple pretreatment a 20 μm pore size mesh filter, proposed by Vermaas *et al.*,[204] to filtrate the biggest particles. Vital *et al.*[205] add to this last a second filter media composed by a 50 cm layer of anthracite (1.2–2.0 mm Ø) on top of a 50 cm layer of sand (0.5–1.0 mm Ø), placed into 11 cm Ø polyvinyl chloride (PVC) pipe. An optimization of the spacers was proposed to reduce the

fouling by Vermass *et al.*[191] where they replaced the traditional spacers and IEMs by profiled membranes, and they found that the pressure drop increased four times slower and the power density remained relatively higher. He *et al.*[206] confirmed this importance of the spacers and proposed a new type with different inlet and outlet to enhance the hydraulic performance and the power density.

Another solution is to modify the anionic exchange membrane surface to make it less attractive to biofouling. Vaselbehagh *et al.*[207] coated a polydopamine layer on the surface of an AEM and found that it reduces bacterial attachment.

Various methods, suggest treating the IEMs with some polymer layer to make them selective for monovalent ions and to reduce the uphill effect and the fouling.[180] From these methods, we can find Gao *et al.*[208] who realized a deposition of two polymers poly(styrenesulfonate) (PSS) and poly(ethyleneimine) (PE) on the surface of an AEM to compare it with commercial one and they showed a good monovalent-anion selectivity comparable, a better anti-organic fouling potential and slightly lower gross power density due to the membrane resistance.

The last strategy is occurred when the fouling is already present. A physical cleaning is used by increasing the pressure or the flow rate for few seconds (a pulse) inside channels to destroy the substances clogging the channels. A chemical washing could be beneficial using some acid and alkaline solutions. To avoid bacteria and algae proliferation, a UV lamp could be installed. With these strategies, they were able to ensure a positive net power density value for more than 18 days using feed from oil well industry.[203]

3.2.7 Scale up. After the lab test, researchers tried to exploit the RED technology at an industrial scale (Table 7). In 2014, a group from a research institution (Wetsus in Netherlands) succeeded to open the first RED plant called REDSTACK with a final power capacity of 50 kW using the freshwater from Lake IJssel and the saltwater of the North Sea available at Afsluitdijk, in Netherlands.

A year after, a pilot plant is started in south of Italy with a RED unit equipped with 50 m^2 of membranes, and working with natural concentrated brine from saltworks basins and brackish water from a shoreline well over a period of five months during the summer. The gross power density was around 0.75–0.85 W m^{-2} corresponding to 40 W with an average net power of 25 W.[194] This pilot[209] has scaled up to reach more than 400 m^2 of total membrane area, delivering a 330 W of gross power capacity which is equivalent to around 0.76 W m^{-2} of power density. After that, a South Korean group built a cell with around 1000 cell pairs with a total area of 250 m^2 and tested it with Ocean lava seawater and wastewater effluent from a sewage treatment plant located beside the sea in Jeju, Korea. The pilot plant was able to produce 95.8 W of power (0.38 W m^{-2}).[213] Recently, Yasukawa *et al.*[211] obtained 0.46 W m^{-2} net power density with a stack of 200 pairs of IEMs, corresponding to 40 m^2 of total effective membrane area, and streams from a seawater reverse osmosis (SWRO) desalination plant, Mamizu Pia (Fukuoka, Japan), and the Wagiro water treatment center (Fukuoka, Japan). The same team evaluated the performance of the RED pilot plant (RED stack) with 299 cell pairs and a 179.4 m^2 membrane effective area, installed in the sea water desalination unit of Okinawa islands in Chatan town, Japan, using one-side monovalent exchange membranes to reduce the uphill effect.[181] Surface water was used as the diluted solution, while the sea water and brine from the desalination process were used as concentrated solution. The maximum gross power output of 171.6 W (0.96 W m^{-2}) for the brine/river water and 110.6 W (0.62 W m^{-2}) for the combination sea-river solutions.

3.2.8 Economic analysis. Several works discussed the economic and financial feasibility of RED for different scenarios. It was shown that the dominating influential factors include the membrane price, which remains very high at present, followed by the inflation, the relatively low experimental power generation and finally the cost of water pretreatment and pumping.[214]

Thin homogeneous membranes with low resistance are generally of high prices (above 80 $ per m^2).[215] In 2007, Turek *et al.*[216] found a very high cost equal to 6.5 $ per kW h by using an experimental power density value of 0.92 W m^{-2} of cell pair and considering a total investment cost of 96 $ per m^2 of installed membrane. In 2010 Post *et al.*[217] fixed a viable power density of 2 W m^{-2} with a membrane price of 2 $ per m^2 and cost of 0.08 $ per kW h for the electricity.

Daniilidis *et al.*[214] suggest that if the membrane technology will be developed by using cheap raw materials and manufacturing procedures in the near future, same as in the ED technology with heterogeneous membrane, allowing a membrane price below 4.3 $ per m^2. A net power density of 2.7 W m^{-2} will be sufficient to start producing energy. And with a LCOE fixed at 0.16 $ per kW h will make RED electricity competitive against conventional and established

Table 7 A summary of RED pilot

Year	σ_H (mS cm^{-1})	σ_L (mS cm^{-1})	Membrane area (m^2)	Membrane pairs number	Gross power density (W m^{-2})	Ref.
2016	150–220	3.4	48.4	125	0.8	194
2017	150–220	3.4	435	1125	0.76	209
2019	52.9–53.8	1.3–5.7	250	1000	0.38	210
2020	83.5–92.3	1.3–2.2	40	200	0.54	211
2021	51.9 ± 1	0.34 ± 0.05	179.4	299	0.62	181
2021	81.9 ± 1	0.34 ± 0.05	179.4	299	0.96	181
2022	31.4 ± 4.1	0.52 ± 0.02	3.1 + 6.2	32 + 64	0.4	212

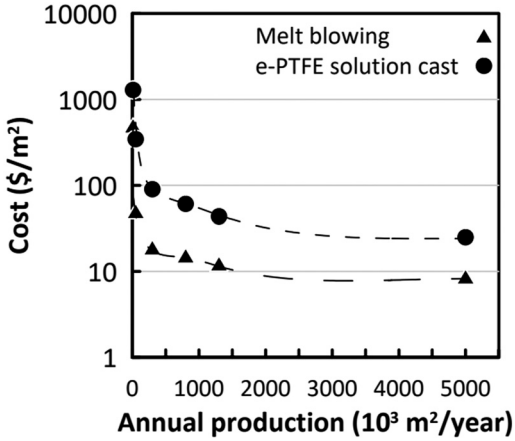

Fig. 19 Cost estimation of PFSA electrolyte membrane produced by two different methods as a function of the total yearly production (figures and captions reproduced from ref. 185 with permission from MDPI, copyright 2020).

renewable technologies. Another study was done by Toupin *et al.*[218] on the cost of Nafion and other perfluorinated sulfonic acid (PFSA) polymer electrolyte membranes. They estimated that with a higher annual production (around 5 million m^2), the cost of 1 m^2 of membrane will be below 10 $ for the melt blowing method[185,218] (see Fig. 19).

In 2019, Giacalone *et al.*[219] estimate the levelized cost of electricity ranging from 0.27 to 0.33 $ per kW h based on membrane cost of 15 $ per m^2, and using brine and freshwater. This cost is lower than the actual electricity prices in certain countries in Europe, that achieve 0.56 $ per kW h last August in Germany. It's worth to note that with the latest events in Ukraine, the fast inflation in the world, and the energy price rise (especially for the natural gas) may make the RED competitive with other power sources.

3.2.9 Miniaturized systems. We have focused in the above approach on the scale up of devices for global energy production. It should be noted that these systems can be miniaturized to power on-board sensors.[220] Sadeglian *et al.*[221] have developed 5 cm diameter cells which miniaturizes a RED system. An IEM is placed between two reservoirs which contain saline solutions of cupric sulphate of different concentrations. The system has a limited production time because it does not include flow or a phase for reconstituting the initial concentration of saline solutions. When the solutions are mixed, it is not possible to return to the initial state. This system makes it possible to obtain a peak power density of 0.7 μW m^{-2} and to deliver an energy of 0.4 mJ cm^{-3}. The previous device has the disadvantage of having a limited power generation time. To overcome this problem, Lin *et al.*[222] have associated an osmotic system composed of two gels containing saline solutions of different concentrations, a selective membrane, faradaic electrodes with a triboelectric system that allows to separate the saline solutions after their mixing. The maximum outpower is 146 μW for an external load resistance of 50 MΩ. This system is efficient and opens the way to use hybrid osmotic–triboelectric systems to power sensors. In the framework seen previously, the triboelectricity is used to reconcentrate the solutions. The advantage compared to a simple triboelectric system is that there is no need for complex impedance matching to perform this charge separation. The results, although preliminary, are comparable to those obtained with piezoelectric[223] or capacitive systems.[2,224] If such systems are proved to work over several cycles, this approach is surely a path for the commercial development of the blue energy. The infrastructure costs are much lower in these miniature devices than those involved in producing energy. Here are a few studies in the literature on the life cycle assessment of blue energy processes, including reverse electrodialysis processes[225–227] Muller *et al.* analyses[225] a functional unit of 1 MW h of net electricity production. They compare their results to wind and solar photovoltaic. Using favorable conditions and assumptions they show that the environmental footprint of the RED is comparable or lower than those of established renewable energy technologies. The main points of focus on RED are the processes associated with membrane manufacturing. The impacts are also greater when lower salt gradients are used due to lower process efficiency. The use of membranes makes eutrophication, ecotoxicity and carcinogenic impacts more significant for RED than for other technologies under certain assumptions.

3.3 Capmixing

Firstly proposed in 2009 by Brogioli,[228] Capmixing is an emerging blue energy harvesting energy with tremendous

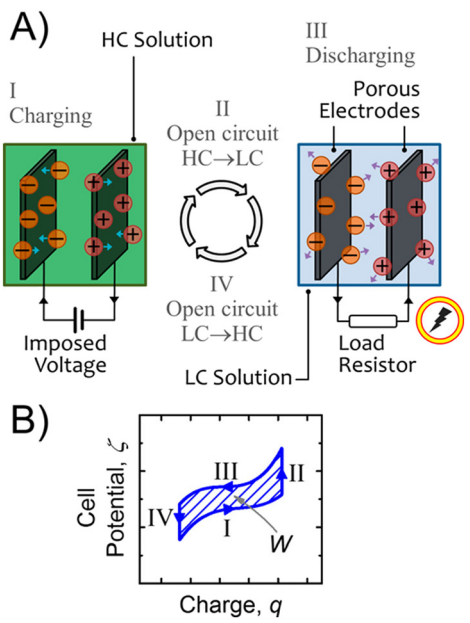

Fig. 20 (A) Illustration of the working principle of capacitive energy extraction based on double layer expansion (CDLE) and (B) the qualitative plot of useful work *W* produced in an unit Capmixing cycle (figures and captions reproduced from ref. 69 with permission from American Chemical Society, copyright 2016).

potential. Unlike PRO and RED where energy conversion is realized through intermediate steps of mechanical turbine systems and electrochemical redox reactions, Capmixing generates electricity directly from a controlled mixing procedure.[69] In a classic configuration of Capmixing illustrated in Fig. 20(A), two porous carbon electrodes are dipped into high concentration solutions at initial state.

It is an energy consuming state where electrodes are charged by an imposed external electric source. Thus, electrical double layers (EDL) are formed near each electrode to maintain a local electron neutrality in the solution.[65] In state II, the system is in open circuit state and the high concentration solution in the system is replaced by solution of lower concentration. As the ionic strength lowering of the electrolyte results in a thickness expansion of the EDL, the overall capacitance of EDL C_{EDL} decreases.[229] Considering the total charges accumulated in the electrodes q remain unchanged, the potential difference between these electrodes DE increases as predicted by the following equation $q = \Delta C_{EDL} \Delta E$. In state III, a load resistor is connected with the Capmixing system. Discharging in electrodes delivers current to produce useful work in the load resistor. At the same time, the thickness of EDL decreases due to the discharging. At final state IV, system switches into open-circuit state and fresh water is replaced by salt water to close the operation loop. As illustrated in Fig. 20(B), the produced work in state III is larger than the energy consumed in state I, a net power is harvested using this so-called capacitive energy extraction based on double layer expansion (CDLE) technology.[68] In the pioneer work of CDLE, Brogioli presented this innovative configuration with a mild power density of 7 mW per square meter of electrodes harvested by two activated carbon porous electrodes.[228] Later, Brogioli *et al.*[230] analyzed the spontaneous potential and the leakage current of different activated carbon electrodes. Based on this analysis, they proposed several suitable couples of activated carbon materials that could possibly enlarge the energy extraction. Using porous carbon electrodes of A-PC-2 and NS30 (two commercial activated carbon films) in CDLE system, a remarkable power density of 50 mW m^{-2} was reported.

In CDLE, capacitive electrodes suffer from self-discharging problems due to faradic reactions on the surface of the carbon. Porada *et al.*[231] summarized these reaction into three types: the first one is the conversion of quinone group on the carbon's surface with two protons to form two hydroquinone. Secondly, the carbon oxidation from carbon to CO_2. And finally, the electrochemical reactions where components in the water react at the carbon surface. Some of them require molecular oxygen in solution. Brogioli *et al.* found that removing oxygen by bubbling nitrogen partially reduces the self-discharge.[232] An alternative solution of using selective faradaic electrodes in the CDLE configuration was proposed in 2011 by Mantia *et al.*[233] The so-called 'Mixing entropy battery' was experimentally demonstrated by using $Na_{2-x}Mn_5O_{10}$ electrode for Na^+ capturing and Ag/AgCl electrode for Cl^- capturing. In this conception, extracted energy from salinity difference is stored inside the bulk crystal structure of the electrode material in chemical energy form. A power density of 138 mW m^{-2} was reported for a salinity gradient of 0.03 M and 1.5 M of NaCl solutions. The main problems of this technique, in addition to the high cost of the electrodes is the relatively short lifespan of the Ag/AgCl electrodes and the low specific capacity of the NMO. Also, the pre-charging step promotes the energy investment.[234] To overcome all that, Ye *et al.*[234] proposed a charge-free MEB with low-cost electrode materials with Prussian blue for the cationic electrode to capture the Na^+, and polypyrrole to capture the Cl^- for anions.

The conventional CDLE configuration requires the external electrical charging system to enable the energy harvesting, which requires higher installation costs and reduce the system efficiency. In 2010, Sales *et al.*[70] proposed to replace auxiliary charging process by using IEMs, so as to use the Donnan potential established across the membrane for system charging. This technology is called capacitive energy extraction based on Donnan potential (CDP). According to their work, Neosepta CEM (or AEM) was placed between the porous carbon electrode and the spacer. While fresh water and salt water were injected alternatively into the spacer, cations and anions were transported through CEM and AEM under the Donnan potential driving force, forming alternative ionic flows (Fig. 21). The initial work of CDP reported a power density of 11.6 mW m^{-2} for solution concentration of 10 mM and 510 mM for fresh water and salt water, respectively. Based on the principle of CDP, modifications of electrodes and membranes were conducted for performance amelioration. Hatzell *et al.*[235] proposed to use flow electrodes containing activated carbons in CDP configuration, which significantly increased the system performance towards 50.9 mW m^{-2}. In 2021, Hwang *et al.*[236] realized systematic research on flow electrodes on varying particle components and concentration, the optimum flow electrodes containing expanded graphite was reported to

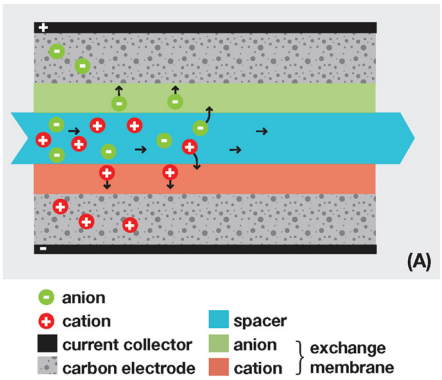

Fig. 21 Illustration of the composition and working principle of capacitive energy extraction based on Donnan potential (CDP). IEMs are used to replace external charging sources so that anions and cations move from spacer channel into porous electrodes (figures and captions reproduced from ref. 70 with permission from American Chemical Society, copyright 2010).

provide a power density of 480 mW m^{-2}. Further optimization on current collector (graphene coated Ti mesh) could even promote the system performance towards 750 mW m^{-2}, according to the recent work of Lee *et al.*[237]

Another emerging strategy similar to CDP is the soft electrodes (SE), where IEMs are replaced by polyelectrolytes to form direct anionic and cationic layers onto electrodes. A pioneering work was realized in 2014 by Ahualli *et al.*[238] by using polyelectrolyte coated carbon electrodes with a power output of 12.1 mW m^{-2}. In 2020, Siekierka *et al.*[239] prepared electrodes coated with EDA and PAA/PMA, reaching a maximum power of 293 mW m^{-2}. However, it is to notice that considerable viscous loss is expected in flow electrode related systems due to the highly viscous properties of flow electrodes.

Numerous theoretical analyses of Capmixing systems were reported,[232,240–242] providing guidelines for optimization of Capmixing. Further strategies, including thermal assisted Capmixing,[243,244] additional charging[245] and module scaling up,[246,247] were also developed for performance enhancement.

3.4 CRED

An innovative configuration combining RED and Capmixing presents a higher power density output with numerous advantages compared with conventional blue energy harvesting technologies. It was firstly reported by Vermaas *et al.*[248] in 2013, suggesting the use of capacitive electrodes in RED configurations (CRED). Such configuration allows the installation of multiple cationic and anionic membrane stacks for higher potential generation and at the same time avoids the redox reactions in the system. In their work, a layer of activated carbon is deposited on a Ti/Pt mesh to form the capacitive electrodes for adsorption and storage of ions. As larger range in voltage and accumulated charge is achieved compared with conventional Capmixing technologies, a maximum power density of 0.9 W m^{-2} can be achieved in cell configuration of a stack of 30 membranes with a salinity difference of 0.017 M and 0.508 M for fresh water and salt water, respectively. Zhan *et al.*[249] proposed

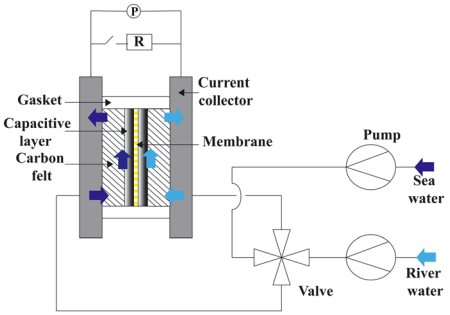

Fig. 22 Scheme of the experimental millifluidic set up used for the salinity gradient harvesting with one membrane and a 6 mm water compartment (figures and captions reproduced from ref. 169 with permission from Elsevier, copyright 2022).

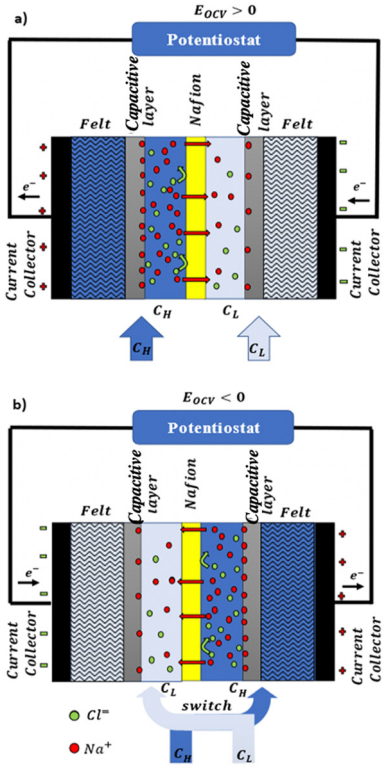

Fig. 23 Illustration of two working regimes for a capacitive salinity-gradient cell before (a) and after (b) water compartment switch (figures and captions reproduced from ref. 169 with permission from Elsevier, copyright 2022).

similar configurations using graphene hydrogel electrodes combined with a single AEM, obtaining an average power density of 0.417 W m^{-2} for a salinity gradient of 0.02 M/0.500 M for NaCl solution.

In 2019, Zhu *et al.*[250] proposed a novel configuration of carbonized peat moss (CPM) electrodes along with a single CEM. They obtained an average power density of 0.95 W m^{-2} for a salinity gradient of 0.017 M and 0.513 M for fresh water and salt water, respectively.

A novel cell design composed of a single selective membrane and two inexpensive capacitive electrodes was presented in the work of Brahmi et Colin (Fig. 22 and 23).[169] A home-made slurry composed of activated carbon particles, carbon nanotubes and PVDF is homogeneously deposited onto a porous carbon electrode to form a capacitive layer. As capacitive electrodes are charged by ion adsorption while immersed in solutions, periodic water compartment switching is necessary to deblock the saturation regime. An alternative capacitive current is generated when an electrical resistance is directly connected to the system. A net power density output of 2 W m^{-2} was reported, with a gradient of 300 (0.017 M/5.1 M) for a simple configuration of a single cationic membrane combined with two inexpensive electrodes. It is to mention that this net power density takes into account the viscous loss in the cell and remains the maximum power density output for CRED systems.

4 Conclusion

In this review, we mainly focus on two different types of water-based energy harvesting systems built on fluidic systems at different scales. Based on the charge separation mechanism, triboelectric energy harvesting systems converts mechanical energy into electrical energy. Osmotic energy harvesting systems realize controlled mixing procedure of solutions of different salinity to recover energies. These two systems have the advantages of being able to be miniaturized[220] as well as being used on a large scale. Though they are not currently in use for electricity production due to many remaining problems, researches of system amelioration are in full development.

We have shown that triboelectric systems can achieve an average power density of a few watt per meter square. The increase of efficiency of triboelectric systems requires a better understanding of charge separation mechanisms but also the implementation of efficient storage processes for the energy generated. Another promising strategy is to investigate in innovative materials. For instance, the composite polymer materials, integrated with conductive particles in order to increase their dielectric constant and their polarizability, could have an important place in future technological developments. It is of great importance to ensure the durability and recycling of these systems. Working with self-healing systems such as vitrimers[251] is a prospect.

The majority of the osmotic energy harvesting systems (PRO, RED and CRED systems) obtain a power density of a few watt per meter square and an energy conversion efficiency below 35%. Though numerous attempts were realized in laboratories and in industrial applications, we now encounter with the bottleneck of performance amelioration, especially for power density and energy conversion efficiency, which remain below the commercialization threshold. The bar of 5 W m^{-2} of net production under industrial production conditions has still not been crossed. The key factor in technology acceleration consists of the amelioration of membrane performance and a significant membrane price reduction. Recent studies have shown that the development of these techniques will not go through the use of membranes resulting from the concepts of nanofluidics or bioinspiration which aroused great interest. To relaunch this track, it is necessary to reduce the polarization effects developed at the entry and exit of membranes with limited energy input. In order to apply these conceptions in membrane engineering, several crucial questions are raised as follows. How to stack nanochannels or slits with large surface charges in space while preventing these nanochannels from interacting with each other? How to optimize electrode arrangement in cell designs so as to avoid the ionic passage through solution compartments (of low ionic conductivity)? How to limit significant pressure drop in energy harvesting systems?

Another promising path, which remains little exploited, is the novel configuration composed of capacitive electrodes and a single membrane. It opens up a novel path of performance enhancement by working on electrode materials. In this context, the use of electrodes exhibiting faradaic surface reactions seems to be a promising track. In terms of device scaling up, it is certain that significant engineering work is required to reduce the filling time during water compartment batching. In general, there is a contribution to be made towards battery technologies to improve these processes.

All these results are very encouraging for powering electronic devices. The applications of the use of saline gradients to supply embedded sensors seem to be a relevant way and can be an important industrial outlet for this technique. The passage to large scales is more futuristic. The economic profitability of triboelectricity is proven. However, it is necessary to improve the lifetimes. The profitability of osmotic energy is less clear. It is true that currently, PRO, RED and Capmixing techniques are not profitable due to the high cost of membranes and water pre-treatments. And the debate of economic viability of osmotic energy harvesting systems has never stopped. However, these economic analyzes should not hinder research. Electricity prices increased by a factor of 20 in 1 year. In such an economic context and because of the scarcity of fossil resources, these techniques will eventually prevail even if they currently remain expensive. The IPCC report reminds us of the importance of taking actions to find solutions for limiting global environmental problems of climate change and greenhouse gas emissions. Our planet is nicknamed the blue planet. 71% of the 509 million m^2 of our planet surface are covered with water,[252] which corresponds to a volume of 140 million km^3. It is therefore a natural idea to develop renewable energies based on salted water resources. Overall, we believe that it is important to continue scientific researches and industrial attempts on these two techniques which could eventually solve the major problem of the 21st century: the ecological transition.

Author contributions

NW, YB, AC wrote, reviewed and edited the manuscript. AC supervised the redaction of the manuscript.

Conflicts of interest

There are no conflicts to declare.

Acknowledgements

NW acknowledges funding from China Scholarship Council (CSC). YB acknowledges funding from the Institut Pierre-Gilles de Gennes (laboratoire d'excellence PSL).

Notes and references

1 S. Priya and D. J. Inman, *Energy harvesting technologies*, Springer, 2009, vol. 21.

2 M. Pruvost, W. J. Smit, C. Monteux, P. Del Corro, I. Dufour, C. Ayela, P. Poulin and A. Colin, *Sci. Rep.*, 2020, **10**, 1–14.
3 D. Guyomar and M. Lallart, *Micromachines*, 2011, **2**, 274–294.
4 A. Harb, *Renewable Energy*, 2011, **36**, 2641–2654.
5 S. E. Skilhagen, J. E. Dugstad and R. J. Aaberg, *Desalination*, 2008, **220**, 476–482.
6 S. Hanson, M. Seok, Y.-S. Lin, Z. Foo, D. Kim, Y. Lee, N. Liu, D. Sylvester and D. Blaauw, *IEEE J. Solid-State Circuits*, 2009, **44**, 1145–1155.
7 S. Jeong, Z. Foo, Y. Lee, J.-Y. Sim, D. Blaauw and D. Sylvester, *IEEE J. Solid-State Circuits*, 2014, **49**, 1682–1693.
8 M. Elimelech and W. A. Phillip, *Science*, 2011, **333**, 712–717.
9 A. Siria, M.-L. Bocquet and L. Bocquet, *Nat. Rev. Chem.*, 2017, **1**, 1–10.
10 S. Lin, X. Chen and Z. L. Wang, *Chem. Rev.*, 2021, **122**, 5209–5232.
11 F.-R. Fan, Z.-Q. Tian and Z. L. Wang, *Nano Energy*, 2012, **1**, 328–334.
12 J. Tian, X. Chen and Z. L. Wang, *Nanotechnology*, 2020, **31**, 242001.
13 Z. L. Wang, *Nano Energy*, 2020, **68**, 104272.
14 Z. L. Wang, *Mater. Today*, 2017, **20**, 74–82.
15 W. Thomson, *Proc. R. Soc. London*, 1868, 67–72.
16 A. G. Marin, W. van Hoeve, P. Garcia-Sanchez, L. Shui, Y. Xie, M. A. Fontelos, J. C. Eijkel, A. van den Berg and D. Lohse, *Lab Chip*, 2013, **13**, 4503–4506.
17 J. P. Tarelho, M. P. S. dos Santos, J. A. Ferreira, A. Ramos, S. Kopyl, S. O. Kim, S. Hong and A. Kholkin, *Mater. Today*, 2018, **21**, 1019–1041.
18 P. Dhiman, F. Yavari, X. Mi, H. Gullapalli, Y. Shi, P. M. Ajayan and N. Koratkar, *Nano Lett.*, 2011, **11**, 3123–3127.
19 J. Yin, X. Li, J. Yu, Z. Zhang, J. Zhou and W. Guo, *Nat. Nanotechnol.*, 2014, **9**, 378–383.
20 J. Yin, Z. Zhang, X. Li, J. Yu, J. Zhou, Y. Chen and W. Guo, *Nat. Commun.*, 2014, **5**, 1–6.
21 S. Lin, L. Zhu, Z. Tang and Z. L. Wang, *Nat. Commun.*, 2022, **13**, 1–9.
22 S. Lin, L. Xu, A. Chi Wang and Z. L. Wang, *Nat. Commun.*, 2020, **11**, 1–8.
23 Z. L. Wang and A. C. Wang, *Mater. Today*, 2019, **30**, 34–51.
24 B. Chen, Y. Xia, R. He, H. Sang, W. Zhang, J. Li, L. Chen, P. Wang, S. Guo and Y. Yin, *et al.*, *Proc. Natl. Acad. Sci. U. S. A.*, 2022, **119**, e2209056119.
25 N. Miljkovic, D. J. Preston, R. Enright and E. N. Wang, *Nat. Commun.*, 2013, **4**, 1–9.
26 Z.-H. Lin, G. Cheng, L. Lin, S. Lee and Z. L. Wang, *Angew. Chem., Int. Ed.*, 2013, **52**, 12545–12549.
27 D. Choi, H. Lee, D. J. Im, I. S. Kang, G. Lim, D. S. Kim and K. H. Kang, *Sci. Rep.*, 2013, **3**, 1–7.
28 J. H. Masliyah and S. Bhattacharjee, *Electrokinetic and colloid transport phenomena*, John Wiley & Sons, 2006.
29 Y. Xie, D. Bos, L. J. De Vreede, H. L. De Boer, M.-J. van der Meulen, M. Versluis, A. J. Sprenkels, A. van den Berg and J. C. Eijkel, *Nat. Commun.*, 2014, **5**, 1–5.
30 W. Xu, H. Zheng, Y. Liu, X. Zhou, C. Zhang, Y. Song, X. Deng, M. Leung, Z. Yang and R. X. Xu, *et al.*, *Nature*, 2020, **578**, 392–396.
31 Q. Sun, D. Wang, Y. Li, J. Zhang, S. Ye, J. Cui, L. Chen, Z. Wang, H.-J. Butt and D. Vollmer, *et al.*, *Nat. Mater.*, 2019, **18**, 936–941.
32 H. Wu, N. Mendel, D. van den Ende, G. Zhou and F. Mugele, *Phys. Rev. Lett.*, 2020, **125**, 078301.
33 X. J. Zhao, G. Zhu, Y. J. Fan, H. Y. Li and Z. L. Wang, *ACS Nano*, 2015, **9**, 7671–7677.
34 S. Jang, M. La, S. Cho, Y. Yun, J. H. Choi, Y. Ra, S. J. Park and D. Choi, *Nano Energy*, 2020, **70**, 104541.
35 G. Zhu, Y. Su, P. Bai, J. Chen, Q. Jing, W. Yang and Z. L. Wang, *ACS Nano*, 2014, **8**, 6031–6037.
36 Y. Su, X. Wen, G. Zhu, J. Yang, J. Chen, P. Bai, Z. Wu, Y. Jiang and Z. L. Wang, *Nano Energy*, 2014, **9**, 186–195.
37 J. Xiong, M.-F. Lin, J. Wang, S. L. Gaw, K. Parida and P. S. Lee, *Adv. Energy Mater.*, 2017, **7**, 1701243.
38 G.-Z. Li, G.-G. Wang, D.-M. Ye, X.-W. Zhang, Z.-Q. Lin, H.-L. Zhou, F. Li, B.-L. Wang and J.-C. Han, *Adv. Electron. Mater.*, 2019, **5**, 1800846.
39 B. K. Yun, H. S. Kim, Y. J. Ko, G. Murillo and J. H. Jung, *Nano Energy*, 2017, **36**, 233–240.
40 Z.-H. Lin, G. Cheng, S. Lee, K. C. Pradel and Z. L. Wang, *Adv. Mater.*, 2014, **26**, 4690–4696.
41 G. Cheng, Z.-H. Lin, Z.-L. Du and Z. L. Wang, *ACS Nano*, 2014, **8**, 1932–1939.
42 Q. Liang, X. Yan, X. Liao and Y. Zhang, *Nano Energy*, 2016, **25**, 18–25.
43 L. Zhao, L. Liu, X. Yang, H. Hong, Q. Yang, J. Wang and Q. Tang, *J. Mater. Chem. A*, 2020, **8**, 7880–7888.
44 R. K. Cheedarala, M. Shahriar, J. H. Ahn, J. Y. Hwang and K. K. Ahn, *Nano Energy*, 2019, **65**, 104017.
45 M. Zhang, C. Bao, C. Hu, Y. Huang, Y. Yang and Y. Su, *Nano Energy*, 2022, 107992.
46 J. H. Ahn, J. Y. Hwang, C. G. Kim, G. H. Nam and K. K. Ahn, *Nano Energy*, 2020, **67**, 104269.
47 S.-H. Kwon, J. Park, W. K. Kim, Y. Yang, E. Lee, C. J. Han, S. Y. Park, J. Lee and Y. S. Kim, *Energy Environ. Sci.*, 2014, **7**, 3279–3283.
48 Z.-H. Lin, G. Cheng, W. Wu, K. C. Pradel and Z. L. Wang, *ACS Nano*, 2014, **8**, 6440–6448.
49 K. Yatsuzuka, Y. Mizuno and K. Asano, *J. Electrost.*, 1994, **32**, 157–171.
50 B. Wang, Y. Wu, Y. Liu, Y. Zheng, Y. Liu, C. Xu, X. Kong, Y. Feng, X. Zhang and D. Wang, *ACS Appl. Mater. Interfaces*, 2020, **12**, 31351–31359.
51 P. Zhao, N. Soin, K. Prashanthi, J. Chen, S. Dong, E. Zhou, Z. Zhu, A. A. Narasimulu, C. D. Montemagno and L. Yu, *et al.*, *ACS Appl. Mater. Interfaces*, 2018, **10**, 5880–5891.
52 C. Cai, B. Luo, Y. Liu, Q. Fu, T. Liu, S. Wang and S. Nie, *Mater. Today*, 2022, **52**, 299–326.
53 BNEF, **https://about.bnef.com/blog/cost-of-new-renewables-temporarily-rises-asinflation-starts-to-bite/**, 2022.
54 Energy.gov, **https://www.energy.gov**, 2022.

55 A. Ahmed, I. Hassan, T. Ibn-Mohammed, H. Mostafa, I. M. Reaney, L. S. Koh, J. Zu and Z. L. Wang, *Energy Environ. Sci.*, 2017, **10**, 653–671.
56 R. Zhang and H. Olin, *ACS Nanosci. Au*, 2021, **2**, 12–31.
57 M. G. Stanford, J. T. Li, Y. Chyan, Z. Wang, W. Wang and J. M. Tour, *ACS Nano*, 2019, **13**, 7166–7174.
58 W. Liu, Z. Wang, G. Wang, Q. Zeng, W. He, L. Liu, X. Wang, Y. Xi, H. Guo and C. Hu, *et al.*, *Nat. Commun.*, 2020, **11**, 1–10.
59 Z. L. Wang, T. Jiang and L. Xu, *Nano Energy*, 2017, **39**, 9–23.
60 X. Wen, W. Yang, Q. Jing and Z. L. Wang, *ACS Nano*, 2014, **8**, 7405–7412.
61 Z. L. Wang, *et al.*, *Nature*, 2017, **542**, 159–160.
62 L. M. Zhang, C. B. Han, T. Jiang, T. Zhou, X. H. Li, C. Zhang and Z. L. Wang, *Nano Energy*, 2016, **22**, 87–94.
63 S. L. Zhang, M. Xu, C. Zhang, Y.-C. Wang, H. Zou, X. He, Z. Wang and Z. L. Wang, *Nano Energy*, 2018, **48**, 421–429.
64 M. Xu, T. Zhao, C. Wang, S. L. Zhang, Z. Li, X. Pan and Z. L. Wang, *ACS Nano*, 2019, **13**, 1932–1939.
65 N. Y. Yip, D. A. Vermaas, K. Nijmeijer and M. Elimelech, *Environ. Sci. Technol.*, 2014, **48**, 4925–4936.
66 R. S. Norman, *Science*, 1974, **186**, 350–352.
67 J. W. Post, H. V. M. Hamelers and C. J. N. Buisman, *Environ. Sci. Technol.*, 2008, **42**, 5785–5790.
68 Z. Jia, B. Wang, S. Song and Y. Fan, *Renewable Sustainable Energy Rev.*, 2014, **31**, 91–100.
69 N. Y. Yip, D. Brogioli, H. V. M. Hamelers and K. Nijmeijer, *Environ. Sci. Technol.*, 2016, **50**, 12072–12094.
70 B. B. Sales, M. Saakes, J. W. Post, C. J. N. Buisman, P. M. Biesheuvel and H. V. M. Hamelers, *Environ. Sci. Technol.*, 2010, **44**, 5661–5665.
71 K. Touati and F. Tadeo, *Int. J. Green Energy*, 2017, **14**, 337–360.
72 S. Sarp, Z. Li and J. Saththasivam, *Desalination*, 2016, **389**, 2–14.
73 F. Helfer, C. Lemckert and Y. G. Anissimov, *J. Membr. Sci.*, 2014, **453**, 337–358.
74 Y. Shi, M. Zhang, H. Zhang, F. Yang, C. Y. Tang and Y. Dong, *Water Res.*, 2021, **189**, 116666.
75 W. Y. Chia, S. R. Chia, K. S. Khoo, K. W. Chew and P. L. Show, *J. Water Process. Eng.*, 2021, **39**, 101758.
76 Q. She, R. Wang, A. G. Fane and C. Y. Tang, *J. Membr. Sci.*, 2016, **499**, 201–233.
77 R. R. Gonzales, A. Abdel-Wahab, S. Adham, D. S. Han, S. Phuntsho, W. Suwaileh, N. Hilal and H. K. Shon, *Desalination*, 2021, **500**, 114841.
78 A. P. Straub, A. Deshmukh and M. Elimelech, *Energy Environ. Sci.*, 2016, **9**, 31–48.
79 S. Lin, A. P. Straub and M. Elimelech, *Energy Environ. Sci.*, 2014, **7**, 2706–2714.
80 B. E. Logan and M. Elimelech, *Nature*, 2012, **488**, 313–319.
81 S. Xu, Y. Liu, Y. Wang, M. Zhang, Q. Xiao and Y. Duan, *Desalination*, 2017, **412**, 39–48.
82 S. Zhao and L. Zou, *J. Membr. Sci.*, 2011, **379**, 459–467.
83 Q. She, X. Jin and C. Y. Tang, *J. Membr. Sci.*, 2012, **401–402**, 262–273.
84 J. Kim, M. J. Park, M. Park, H. K. Shon, S.-H. Kim and J. H. Kim, *Desalination*, 2016, **389**, 207–214.
85 N. Y. Yip and M. Elimelech, *Environ. Sci. Technol.*, 2013, **47**, 12607–12616.
86 M. Tawalbeh, A. Al-Othman, N. Abdelwahab, A. H. Alami and A. G. Olabi, *Renewable Sustainable Energy Rev.*, 2021, **138**, 110492.
87 S. Loeb, F. Van Hessen and D. Shahaf, *J. Membr. Sci.*, 1976, **1**, 249–269.
88 G. D. Mehta, *J. Membr. Sci.*, 1982, **10**, 3–19.
89 A. Achilli, T. Y. Cath and A. E. Childress, *J. Membr. Sci.*, 2009, **343**, 42–52.
90 N. Akther, A. Sodiq, A. Giwa, S. Daer, H. A. Arafat and S. W. Hasan, *Chem. Eng. J.*, 2015, **281**, 502–522.
91 Y. C. Kim and M. Elimelech, *J. Membr. Sci.*, 2013, **429**, 330–337.
92 S. L. Plata and A. E. Childress, *Desalination*, 2019, **467**, 51–56.
93 N. AlZainati, H. Saleem, A. Altaee, S. J. Zaidi, M. Mohsen, A. Hawari and G. J. Millar, *J. Water Process. Eng.*, 2021, **40**, 101950.
94 N. Y. Yip, A. Tiraferri, W. A. Phillip, J. D. Schiffman, L. A. Hoover, Y. C. Kim and M. Elimelech, *Environ. Sci. Technol.*, 2011, **45**, 4360–4369.
95 G. Han, S. Zhang, X. Li and T.-S. Chung, *J. Membr. Sci.*, 2013, **440**, 108–121.
96 X. Li, S. Zhang, F. Fu and T.-S. Chung, *J. Membr. Sci.*, 2013, **434**, 204–217.
97 M. Son, H. Park, L. Liu, H. Choi, J. H. Kim and H. Choi, *Chem. Eng. J.*, 2016, **284**, 68–77.
98 J. Wei, Y. Li, L. Setiawan and R. Wang, *J. Membr. Sci.*, 2016, **511**, 54–64.
99 N.-N. Bui and J. R. McCutcheon, *Environ. Sci. Technol.*, 2014, **48**, 4129–4136.
100 M. Tian, R. Wang, K. Goh, Y. Liao and A. G. Fane, *J. Membr. Sci.*, 2015, **486**, 151–160.
101 S. Lim, M. J. Park, S. Phuntsho, A. Mai-Prochnow, A. B. Murphy, D. Seo and H. Shon, *J. Membr. Sci.*, 2018, **564**, 382–393.
102 R. R. Gonzales, M. J. Park, T.-H. Bae, Y. Yang, A. Abdel-Wahab, S. Phuntsho and H. K. Shon, *Desalination*, 2019, **459**, 10–19.
103 S. J. Kwon, K. Park, D. Y. Kim, M. Zhan, S. Hong and J.-H. Lee, *J. Membr. Sci.*, 2021, **619**, 118796.
104 J. H. Kim, S. J. Moon, S. H. Park, M. Cook, A. G. Livingston and Y. M. Lee, *J. Membr. Sci.*, 2018, **550**, 322–331.
105 S. J. Moon, J. H. Kim, J. G. Seong, W. H. Lee, S. H. Park, S. H. Noh, J. H. Kim and Y. M. Lee, *J. Membr. Sci.*, 2020, **607**, 118120.
106 H. W. Chung, J. Swaminathan, L. D. Banchik and J. H. Lienhard, *Desalination*, 2018, **448**, 13–20.
107 Y. C. Kim and M. Elimelech, *Environ. Sci. Technol.*, 2012, **46**, 4673–4681.
108 Q. She, D. Hou, J. Liu, K. H. Tan and C. Y. Tang, *J. Membr. Sci.*, 2013, **445**, 170–182.

109 E. Sivertsen, T. Holt, W. Thelin and G. Brekke, *Desalination*, 2013, **312**, 107–123.
110 S. Chou, R. Wang, L. Shi, Q. She, C. Tang and A. G. Fane, *J. Membr. Sci.*, 2012, **389**, 25–33.
111 S. Chou, R. Wang and A. G. Fane, *J. Membr. Sci.*, 2013, **448**, 44–54.
112 P. G. Ingole, W. Choi, K.-H. Kim, H.-D. Jo, W.-K. Choi, J.-S. Park and H.-K. Lee, *Desalination*, 2014, **345**, 136–145.
113 P. G. Ingole, W. Choi, K. H. Kim, C. H. Park, W. K. Choi and H. K. Lee, *Chem. Eng. J.*, 2014, **243**, 137–146.
114 F.-J. Fu, S.-P. Sun, S. Zhang and T.-S. Chung, *J. Membr. Sci.*, 2014, **469**, 488–498.
115 X. Li, T. Cai and T.-S. Chung, *Environ. Sci. Technol.*, 2014, **48**, 9898–9907.
116 P. G. Ingole, K. H. Kim, C. H. Park, W. K. Choi and H. K. Lee, *RSC Adv.*, 2014, **4**, 51430–51439.
117 Y. Zhang, J. L. Li, T. Cai, Z. L. Cheng, X. Li and T.-S. Chung, *J. Membr. Sci.*, 2018, **563**, 521–530.
118 D. L. Zhao, S. Das and T.-S. Chung, *Environ. Sci. Technol.*, 2017, **51**, 14016–14023.
119 W. Gai, D. L. Zhao and T.-S. Chung, *J. Membr. Sci.*, 2018, **551**, 94–102.
120 M. J. Park, S. Lim, R. R. Gonzales, S. Phuntsho, D. S. Han, A. Abdel-Wahab, S. Adham and H. K. Shon, *Desalination*, 2019, **464**, 63–75.
121 D. Zhao, G. Qiu, X. Li, C. Wan, K. Lu and T.-S. Chung, *Water Res.*, 2016, **104**, 389–396.
122 N. L. Le, N. M. S. Bettahalli, S. P. Nunes and T.-S. Chung, *J. Membr. Sci.*, 2016, **505**, 157–166.
123 G. Han, P. Wang and T.-S. Chung, *Environ. Sci. Technol.*, 2013, **47**, 8070–8077.
124 S. Zhang, F. Fu and T.-S. Chung, *Chem. Eng. Sci.*, 2013, **87**, 40–50.
125 X. Li, T.-S. Chung and T.-S. Chung, *AIChE J.*, 2013, **59**, 4749–4761.
126 X. Song, Z. Liu and D. D. Sun, *Energy Environ. Sci.*, 2013, **6**, 1199.
127 Y. Cui, X.-Y. Liu and T.-S. Chung, *Chem. Eng. J.*, 2014, **242**, 195–203.
128 A. P. Straub, N. Y. Yip and M. Elimelech, *Environ. Sci. Technol. Lett.*, 2014, **1**, 55–59.
129 Y. Li, R. Wang, S. Qi and C. Tang, *J. Membr. Sci.*, 2015, **488**, 143–153.
130 Q. She, J. Wei, N. Ma, V. Sim, A. G. Fane, R. Wang and C. Y. Tang, *J. Membr. Sci.*, 2016, **504**, 75–88.
131 J. A. Idarraga-Mora, D. A. Ladner and S. M. Husson, *J. Membr. Sci.*, 2018, **549**, 251–259.
132 Y. Sun, L. Cheng, T. Shintani, Y. Tanaka, T. Takahashi, T. Itai, S. Wang, L. Fang and H. Matsuyama, *Ind. Eng. Chem. Res.*, 2018, **57**, 13528–13538.
133 X. Tong, X. Wang, S. Liu, H. Gao, C. Xu, J. Crittenden and Y. Chen, *Carbon*, 2018, **138**, 410–418.
134 S. J. Moon, S. M. Lee, J. H. Kim, S. H. Park, H. H. Wang, J. H. Kim and Y. M. Lee, *Desalination*, 2020, **483**, 114409.
135 F.-J. Fu, S. Zhang, S.-P. Sun, K.-Y. Wang and T.-S. Chung, *J. Membr. Sci.*, 2013, **443**, 144–155.
136 S.-P. Sun and T.-S. Chung, *Environ. Sci. Technol.*, 2013, **47**, 13167–13174.
137 S. Zhang, P. Sukitpaneenit and T.-S. Chung, *Chem. Eng. J.*, 2014, **241**, 457–465.
138 G. Han and T.-S. Chung, *AIChE J.*, 2014, **60**, 1107–1119.
139 G. Han, Q. Ge and T.-S. Chung, *Appl. Energy*, 2014, **132**, 383–393.
140 S. C. Chen, C. F. Wan and T.-S. Chung, *J. Membr. Sci.*, 2015, **479**, 190–203.
141 F.-J. Fu, S. Zhang and T.-S. Chung, *Desalination*, 2015, **376**, 73–81.
142 Z. L. Cheng, X. Li, Y. D. Liu and T.-S. Chung, *J. Membr. Sci.*, 2016, **506**, 119–129.
143 W. Gai, X. Li, J. Y. Xiong, C. F. Wan and T.-S. Chung, *J. Membr. Sci.*, 2016, **516**, 104–112.
144 L. Zhang, Q. She, R. Wang, S. Wongchitphimon, Y. Chen and A. G. Fane, *Desalination*, 2016, **389**, 119–128.
145 Y. Chen, L. Setiawan, S. Chou, X. Hu and R. Wang, *J. Membr. Sci.*, 2016, **503**, 90–100.
146 N. Lieu Le, M. Quilitzsch, H. Cheng, P.-Y. Hong, M. Ulbricht, S. P. Nunes and T.-S. Chung, *J. Membr. Sci.*, 2017, **522**, 1–11.
147 Z. L. Cheng, X. Li, Y. Feng, C. F. Wan and T.-S. Chung, *J. Membr. Sci.*, 2017, **524**, 97–107.
148 C. F. Wan, B. Li, T. Yang and T.-S. Chung, *Sep. Purif. Technol.*, 2017, **172**, 32–42.
149 G. Han, Z. L. Cheng and T.-S. Chung, *J. Membr. Sci.*, 2017, **523**, 497–504.
150 C. F. Wan, T. Yang, W. Gai, Y. D. Lee and T.-S. Chung, *J. Membr. Sci.*, 2018, **555**, 388–397.
151 Y. Chen, C. H. Loh, L. Zhang, L. Setiawan, Q. She, W. Fang, X. Hu and R. Wang, *J. Membr. Sci.*, 2018, **548**, 398–407.
152 Y. Li, S. Zhao, L. Setiawan, L. Zhang and R. Wang, *J. Membr. Sci.*, 2018, **550**, 163–172.
153 Y. H. Cho, S. D. Kim, J. F. Kim, H.-G. Choi, Y. Kim, S.-E. Nam, Y.-I. Park and H. Park, *J. Membr. Sci.*, 2019, **579**, 329–341.
154 R. R. Gonzales, Y. Yang, M. J. Park, T.-H. Bae, A. Abdel-Wahab, S. Phuntsho and H. K. Shon, *Desalination*, 2020, **496**, 114756.
155 K. Gerstandt, K. V. Peinemann, S. E. Skilhagen, T. Thorsen and T. Holt, *Desalination*, 2008, **224**, 64–70.
156 S. AL Mashrafi, N. Diaz-Elsayed, J. Benjamin, M. E. Arias and Q. Zhang, *Desalination*, 2022, **537**, 115869.
157 Q. A. Khasawneh, B. Tashtoush, A. Nawafleh and B. Kan'an, *Energies*, 2018, **11**, 3118.
158 T. N. American, *Crown Princess of Norway to Open the World's First Osmotic Power Plant*, **https://www.norwegianamerican.com/crown-princess-ofnorway-to-open-the-worlds-first-osmotic-power-plant/**, 2009.
159 C. Lee, S. H. Chae, E. Yang, S. Kim, J. H. Kim and I. S. Kim, *Desalination*, 2020, **491**, 114501.
160 *Osmotic Power Plant Opened*, REUK.Co.Uk.
161 M. Kurihara and H. Takeuchi, *Water*, 2018, **10**, 48.
162 R. E. Pattle, *Nature*, 1954, **174**, 660–660.
163 R. E. Lacey, *Ocean Eng.*, 1980, **7**, 1–47.

164 A. Galama, J. Post, H. Hamelers, V. Nikonenko and P. Biesheuvel, *J. Membr. Sci. Res.*, 2016, **2**, 128–140.
165 T. Teorell, *Proc. Soc. Exp. Biol. Med.*, 1935, **33**, 282–285.
166 F. Morrison Jr and J. Osterle, *J. Chem. Phys.*, 1965, **43**, 2111–2115.
167 A. Siria, P. Poncharal, A.-L. Biance, R. Fulcrand, X. Blase, S. T. Purcell and L. Bocquet, *Nature*, 2013, **494**, 455–458.
168 Z. Tang, Q.-A. Huang, Y.-J. Wang, F. Zhang, W. Li, A. Li, L. Zhang and J. Zhang, *J. Power Sources*, 2020, **468**, 228361.
169 Y. Brahmi and A. Colin, *Energy Convers. Manage.*, 2022, **254**, 115297.
170 J. Veerman, M. Saakes, S. J. Metz and G. J. Harmsen, *J. Appl. Electrochem.*, 2010, **40**, 1461–1474.
171 J. Jagur-Grodzinski and R. Kramer, *Ind. Eng. Chem. Process Des. Dev.*, 1986, **25**, 443–449.
172 J. Veerman, M. Saakes, S. J. Metz and G. J. Harmsen, *Environ. Sci. Technol.*, 2010, **44**, 9207–9212.
173 A. Daniilidis, D. A. Vermaas, R. Herber and K. Nijmeijer, *Renewable Energy*, 2014, **64**, 123–131.
174 J. Veerman, R. M. de Jong, M. Saakes, S. J. Metz and G. J. Harmsen, *J. Membr. Sci.*, 2009, **343**, 7–15.
175 J. Veerman and D. Vermaas, *Sustainable Energy from Salinity Gradients*, Elsevier, 2016, pp. 77–133.
176 D. A. Vermaas, M. Saakes and K. Nijmeijer, *Environ. Sci. Technol.*, 2011, **45**, 7089–7095.
177 M. Turek, B. Bandura and P. Dydo, *Desalination*, 2008, **221**, 462–466.
178 R. Audinos, *J. Power Sources*, 1983, **10**, 203–217.
179 P. Dlugolecki, K. Nymeijer, S. Metz and M. Wessling, *J. Membr. Sci.*, 2008, **319**, 214–222.
180 J. Moreno, V. Díez, M. Saakes and K. Nijmeijer, *J. Membr. Sci.*, 2018, **550**, 155–162.
181 S. Mehdizadeh, Y. Kakihana, T. Abo, Q. Yuan and M. Higa, *Membranes*, 2021, **11**, 27.
182 M. Tedesco, E. Brauns, A. Cipollina, G. Micale, P. Modica, G. Russo and J. Helsen, *J. Membr. Sci.*, 2015, **492**, 9–20.
183 J. G. Hong and Y. Chen, *J. Membr. Sci.*, 2014, **460**, 139–147.
184 D. A. Vermaas, J. Veerman, M. Saakes and K. Nijmeijer, *Energy Environ. Sci.*, 2014, **7**, 1434–1445.
185 A. H. Avci, D. A. Messana, S. Santoro, R. A. Tufa, E. Curcio, G. Di Profio and E. Fontananova, *Membranes*, 2020, **10**, 168.
186 E. Güler, R. Elizen, D. A. Vermaas, M. Saakes and K. Nijmeijer, *J. Membr. Sci.*, 2013, **446**, 266–276.
187 T. Rijnaarts, J. Moreno, M. Saakes, W. M. de Vos and K. Nijmeijer, *Colloids Surf., A*, 2019, **560**, 198–204.
188 M. Y. Kariduraganavar, R. K. Nagarale, A. A. Kittur and S. S. Kulkarni, *Desalination*, 2006, **197**, 225–246.
189 N. D. Pismenskaya, E. V. Pokhidnia, G. Pourcelly and V. V. Nikonenko, *J. Membr. Sci.*, 2018, **566**, 54–68.
190 J. Veerman, M. Saakes, S. Metz and G. Harmsen, *J. Membr. Sci.*, 2009, **327**, 136–144.
191 D. A. Vermaas, M. Saakes and K. Nijmeijer, *J. Membr. Sci.*, 2011, **385–386**, 234–242.
192 E. Guler, Y. Zhang, M. Saakes and K. Nijmeijer, *ChemSusChem*, 2012, **5**, 2262–2270.
193 D. A. Vermaas, M. Saakes and K. Nijmeijer, *J. Membr. Sci.*, 2014, **453**, 312–319.
194 M. Tedesco, C. Scalici, D. Vaccari, A. Cipollina, A. Tamburini and G. Micale, *J. Membr. Sci.*, 2016, **500**, 33–45.
195 A. H. Avci, R. A. Tufa, E. Fontananova, G. Di Profio and E. Curcio, *Energy*, 2018, **165**, 512–521.
196 H. Kim, S. Yang, J. Choi, J.-O. Kim and N. Jeong, *Desalination*, 2021, **497**, 114676.
197 J. Gao, X. Liu, Y. Jiang, L. Ding, L. Jiang and W. Guo, *Small*, 2019, **15**, 1804279.
198 X. Liu, M. He, D. Calvani, H. Qi, K. B. Gupta, H. J. de Groot, G. Sevink, F. Buda, U. Kaiser and G. F. Schneider, *Nat. Nanotechnol.*, 2020, **15**, 307–312.
199 C. Li, L. Wen, X. Sui, Y. Cheng, L. Gao and L. Jiang, *Sci. Adv.*, 2021, **7**, eabg2183.
200 A. A. Moya, *J. Membr. Sci.*, 2020, **598**, 117784.
201 R. A. Tufa, E. Curcio, W. van Baak, J. Veerman, S. Grasman, E. Fontananova and G. D. Profio, *RSC Adv.*, 2014, **4**, 42617–42623.
202 R. S. Kingsbury, F. Liu, S. Zhu, C. Boggs, M. D. Armstrong, D. F. Call and O. Coronell, *J. Membr. Sci.*, 2017, **541**, 621–632.
203 A. Cosenza, G. Campisi, F. Giacalone, S. Randazzo, A. Cipollina, A. Tamburini and G. Micale, *Energies*, 2022, **15**, 4177.
204 D. A. Vermaas, D. Kunteng, M. Saakes and K. Nijmeijer, *Water Res.*, 2013, **47**, 1289–1298.
205 B. Vital, E. V. Torres, T. Sleutels, M. C. Gagliano, M. Saakes and H. V. M. Hamelers, *Desalination*, 2021, **518**, 115277.
206 Z. He, X. Gao, Y. Zhang, Y. Wang and J. Wang, *Desalin. Water Treat.*, 2016, **57**, 28176–28186.
207 M. Vaselbehagh, H. Karkhanechi, R. Takagi and H. Matsuyama, *J. Membr. Sci.*, 2017, **530**, 232–239.
208 H. Gao, B. Zhang, X. Tong and Y. Chen, *J. Membr. Sci.*, 2018, **567**, 68–75.
209 M. Tedesco, A. Cipollina, A. Tamburini and G. Micale, *J. Membr. Sci.*, 2017, **522**, 226–236.
210 J.-Y. Nam, K.-S. Hwang, H.-C. Kim, H. Jeong, H. Kim, E. Jwa, S. Yang, J. Choi, C.-S. Kim, J.-H. Han and N. Jeong, *Water Res.*, 2019, **148**, 261–271.
211 M. Yasukawa, S. Mehdizadeh, T. Sakurada, T. Abo, M. Kuno and M. Higa, *Desalination*, 2020, **491**, 114449.
212 C. Simões, B. Vital, T. Sleutels, M. Saakes and W. Brilman, *Chem. Eng. J.*, 2022, **450**, 138412.
213 J.-Y. Nam, K.-S. Hwang, H.-C. Kim, H. Jeong, H. Kim, E. Jwa, S. Yang, J. Choi, C.-S. Kim, J.-H. Han and N. Jeong, *Water Res.*, 2019, **148**, 261–271.
214 A. Daniilidis, R. Herber and D. A. Vermaas, *Appl. Energy*, 2014, **119**, 257–265.
215 R. A. Tufa, S. Pawlowski, J. Veerman, K. Bouzek, E. Fontananova, G. di Profio, S. Velizarov, J. Goulão Crespo, K. Nijmeijer and E. Curcio, *Appl. Energy*, 2018, **225**, 290–331.
216 M. Turek and B. Bandura, *Desalination*, 2007, **205**, 67–74.
217 J. W. Post, C. H. Goeting, J. Valk, S. Goinga, J. Veerman, H. V. M. Hamelers and P. J. F. M. Hack, *Desalin. Water Treat.*, 2010, **16**, 182–193.

218 M. Toupin, K. Malek and A. Mokrini, *World Electr. Veh. J.*, 2016, **8**, 431–442.
219 F. Giacalone, M. Papapetrou, G. Kosmadakis, A. Tamburini, G. Micale and A. Cipollina, *Energy*, 2019, **181**, 532–547.
220 W.-S. Hsu, A. Preet, T.-Y. Lin and T.-E. Lin, *Molecules*, 2021, **26**, 5469.
221 R. B. Sadeglian, O. Pantchenko, D. Tate and A. Shakouri, *Appl. Phys. Lett.*, 2011, **99**, 173702.
222 Z.-H. Lin, W.-S. Hsu, A. Preet, L.-H. Yeh, Y.-H. Chen, Y.-P. Pao, S.-F. Lin, S. Lee, J.-C. Fan and L. Wang, *et al.*, *Nano Energy*, 2021, **79**, 105440.
223 S. Roundy, P. K. Wright and J. Rabaey, *Comput. Commun.*, 2003, **26**, 1131–1144.
224 M. Pruvost, W. J. Smit, C. Monteux, P. Poulin and A. Colin, *Multifunct. Mater.*, 2018, **1**, 015004.
225 K. E. Mueller, J. T. Thomas, J. X. Johnson, J. F. DeCarolis and D. F. Call, *J. Ind. Ecol.*, 2021, **25**, 1194–1206.
226 C. Tristán, M. Rumayor, A. Dominguez-Ramos, M. Fallanza, R. Ibáñez and I. Ortiz, *Sustainable Energy Fuels*, 2020, **4**, 4273–4284.
227 F. Giacalone, P. Catrini, A. Tamburini, A. Cipollina, A. Piacentino and G. Micale, *Energy Convers. Manage.*, 2018, **164**, 588–602.
228 D. Brogioli, *Phys. Rev. Lett.*, 2009, **103**, 058501.
229 P. Sharma and T. S. Bhatti, *Energy Convers. Manage.*, 2010, **51**, 2901–2912.
230 D. Brogioli, R. Ziano, R. A. Rica, D. Salerno, O. Kozynchenko, H. V. M. Hamelers and F. Mantegazza, *Energy Environ. Sci.*, 2012, **5**, 9870–9880.
231 S. Porada, R. Zhao, A. van der Wal, V. Presser and P. Biesheuvel, *Prog. Mater. Sci.*, 2013, **58**, 1388–1442.
232 D. Brogioli, R. Ziano, R. Rica, D. Salerno and F. Mantegazza, *J. Colloid Interface Sci.*, 2013, **407**, 457–466.
233 F. La Mantia, M. Pasta, H. D. Deshazer, B. E. Logan and Y. Cui, *Nano Lett.*, 2011, **11**, 1810–1813.
234 M. Ye, M. Pasta, X. Xie, K. L. Dubrawski, J. Xu, C. Liu, Y. Cui and C. S. Criddle, *ACS Omega*, 2019, **4**, 11785–11790.
235 M. C. Hatzell, K. B. Hatzell and B. E. Logan, *Environ. Sci. Technol. Lett.*, 2014, **1**, 474–478.
236 I. Hwang, D. Lee, Y. Jung, K. Park, Y.-G. Jung, D. Kim, G.-H. Cho, S.-I. Jeon, Y.-K. Byeun, U. Paik, S. Yang and T. Song, *ACS Sustainable Chem. Eng.*, 2021, **9**, 13514–13525.
237 D. Lee, J. S. Roh, I. Hwang, Y. Jung, H. Lee, I. W. Ock, S. Kim, S. Sun, S. Yang, H. B. Park, U. Paik and T. Song, *ACS Sustainable Chem. Eng.*, 2022, **10**, 7625–7634.
238 S. Ahualli, M. L. Jiménez, M. M. Fernández, G. Iglesias, D. Brogioli and Á. V. Delgado, *Phys. Chem. Chem. Phys.*, 2014, **16**, 25241–25246.
239 A. Siekierka, K. Smolínska-Kempisty and M. Bryjak, *Desalination*, 2020, **495**, 114670.
240 R. A. Rica, R. Ziano, D. Salerno, F. Mantegazza and D. Brogioli, *Phys. Rev. Lett.*, 2012, **109**, 156103.
241 X. Kong, A. Gallegos, D. Lu, Z. Liu and J. Wu, *Phys. Chem. Chem. Phys.*, 2015, **17**, 23970–23976.
242 M. Nasir, Y. Nakanishi, A. Patmonoaji and T. Suekane, *Renewable Energy*, 2020, **155**, 278–285.
243 D. Moreno and M. C. Hatzell, *ACS Sustainable Chem. Eng.*, 2019, **7**, 11334–11340.
244 S. Ahualli, M. L. Jiménez, Z. Amador, M. M. Fernández, G. R. Iglesias and A. V. Delgado, *Sustainable Energy Fuels*, 2021, **5**, 3321–3329.
245 Z. Zou, L. Liu, S. Meng and X. Bian, *Energy Rep.*, 2022, **8**, 7325–7335.
246 G. R. Iglesias, S. Ahualli, M. M. Fernández, M. L. Jiménez and Á. V. Delgado, *J. Power Sources*, 2016, **318**, 283–290.
247 F. Liu, T. F. W. Donkers, R. M. Wagterveld, O. Schaetzle, M. Saakes, C. J. N. Buisman and H. V. M. Hamelers, *Electrochim. Acta*, 2016, **187**, 104–112.
248 D. A. Vermaas, S. Bajracharya, B. B. Sales, M. Saakes, B. Hamelers and K. Nijmeijer, *Energy Environ. Sci.*, 2013, **6**, 643–651.
249 F. Zhan, Z. Wang, T. Wu, Q. Dong, C. Zhao, G. Wang and J. Qiu, *J. Mater. Chem. A*, 2018, **6**, 4981–4987.
250 H. Zhu, W. Xu, G. Tan, E. Whiddon, Y. Wang, C. G. Arges and X. Zhu, *Electrochim. Acta*, 2019, **294**, 240–248.
251 M. Röttger, T. Domenech, R. van der Weegen, A. Breuillac, R. Nicolaÿ and L. Leibler, *Science*, 2017, **356**, 62–65.
252 B. Nath, *Resonance*, 2019, **24**, 575–582.